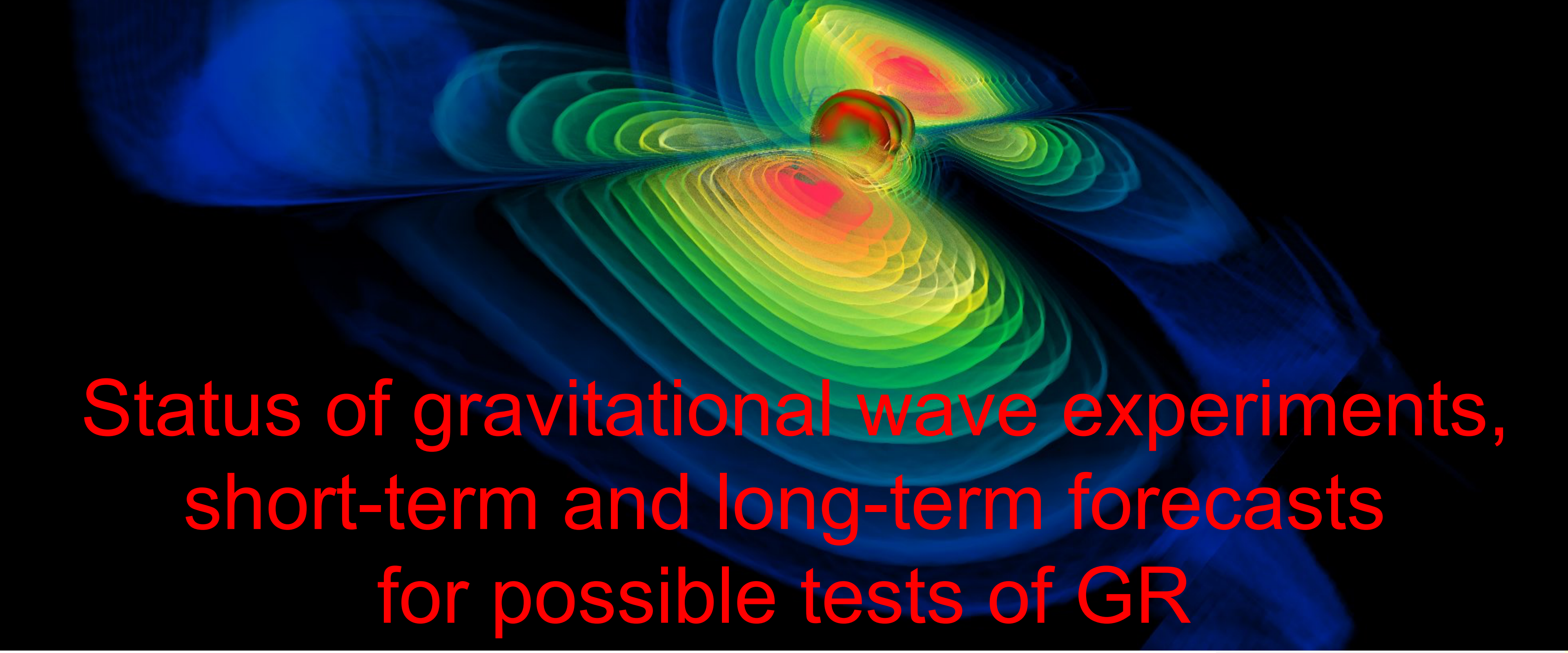

Status of gravitational wave experiments, short-term and long-term forecasts for possible tests of GR

László Árpád GERGELY

University of Szeged

COST Action CA18108 QG-MM: "Quantum gravity phenomenology in the multi-messenger approach" workshop

2 October 2019, Aula Magna, Casa de Convalescencia, Barcelona

The success of general relativity

Solar System & other tests

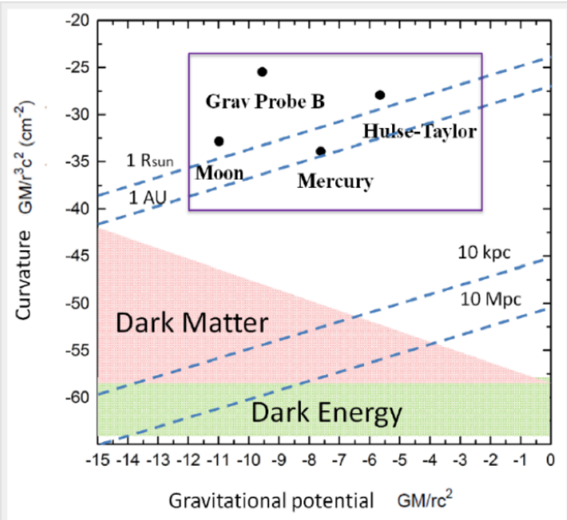

Fig 1: Tests of General Relativity on various scales. The vertical axis is the spacetime curvature and the horizontal axis is the gravitational potential. The blue dotted lines indicate typical length scales. Modified from Psaltis arXiv:0806.1531. GR is well tested at solar system scales and also by binary pulsars (within the purple box). However, outside this region, gravity is not tested by conventional methods.

www.icg.port.ac.uk/cosmological-tests-of-gravity/

Hulse-Taylor pulsar

Comparison between observations of the binary pulsar PSR1913+16, and the prediction of general relativity based on loss of orbital energy via gravitational waves

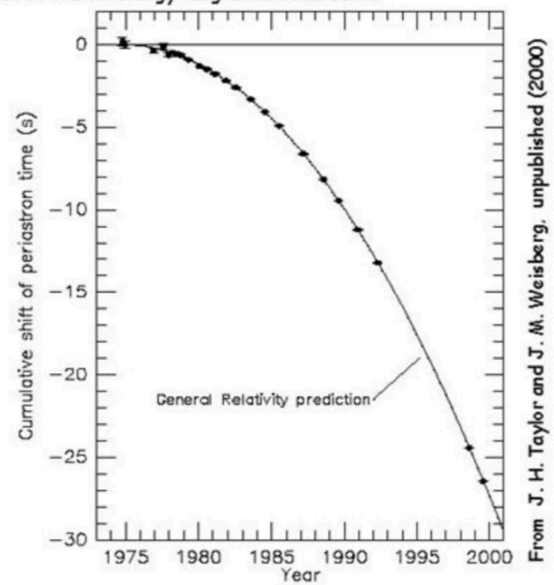

40s change in 30 years!! (4×10^{-8})

Gravity Probe B

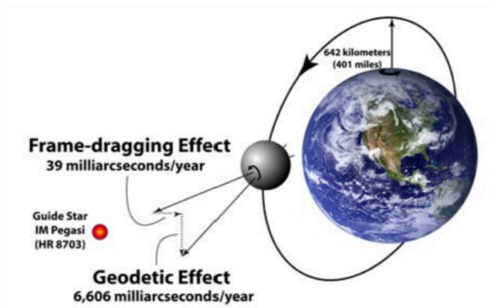

Everitt, C.W.F.; Parkinson, B.W. (2009). "Gravity Probe B Science Results—NASA Final Report"

Double pulsar

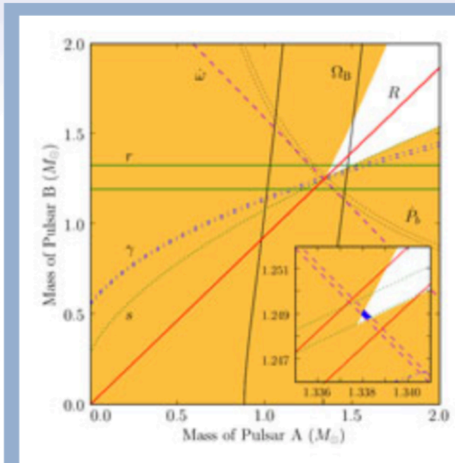

Mass-mass diagram illustrating the present tests constraining general relativity in the double pulsar PSR J0737-3039A/B. Because observations are consistent with general relativity, all lines intersect at common values of masses. Shaded orange regions are unphysical solutions because $\sin i \le 1$, where i is the orbital inclination. The mass ratio, R, and five post-Keplerian parameters (s and r, Shapiro delay shape and range; ω , periastron advance; $\dot{P}_b$, orbital period decay due to the emission of gravitational waves; and γ, gravitational redshift and time dilation) were reported by Kramer et al. (2006). The spin precession rate of pulsar B, Ω_B, yields a new constraint on the mass-mass diagram.

https://www.nrao.edu/news/newsletters/enews/enews_1_2/einstein.shtml

The supermassive black hole at the center of our Galaxy

Large curvature→ black holes

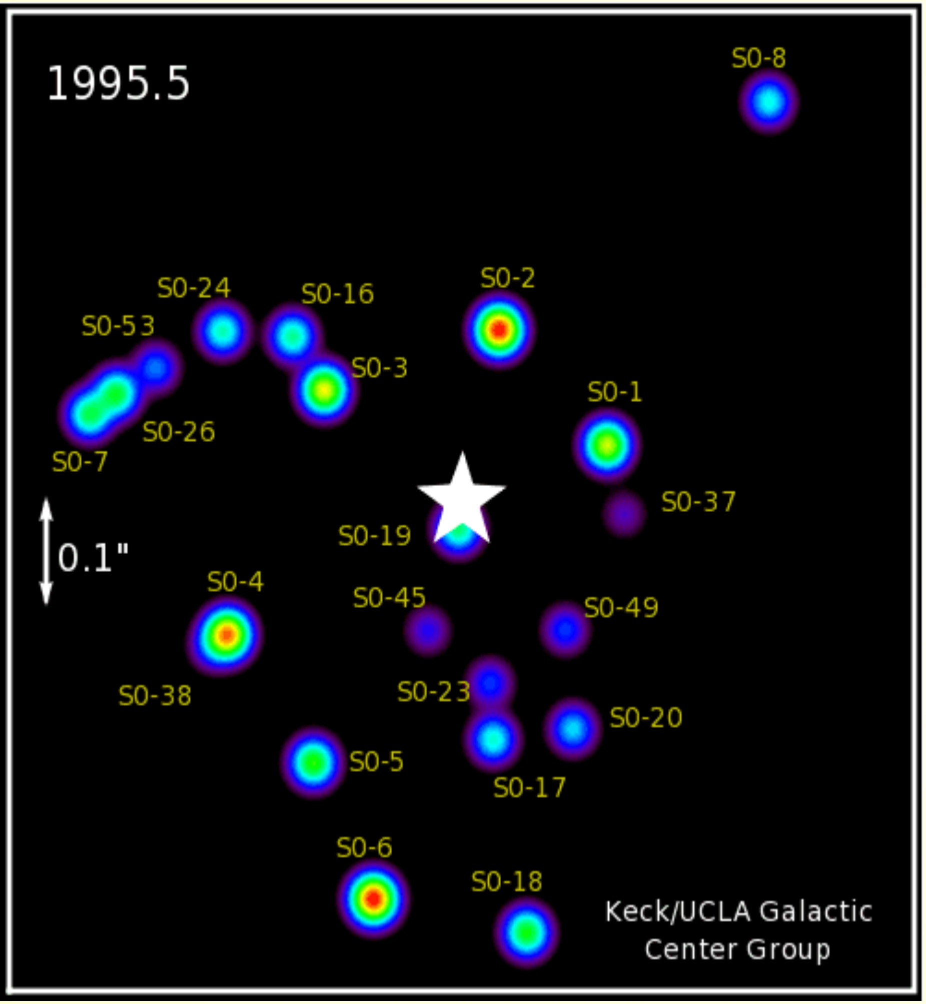

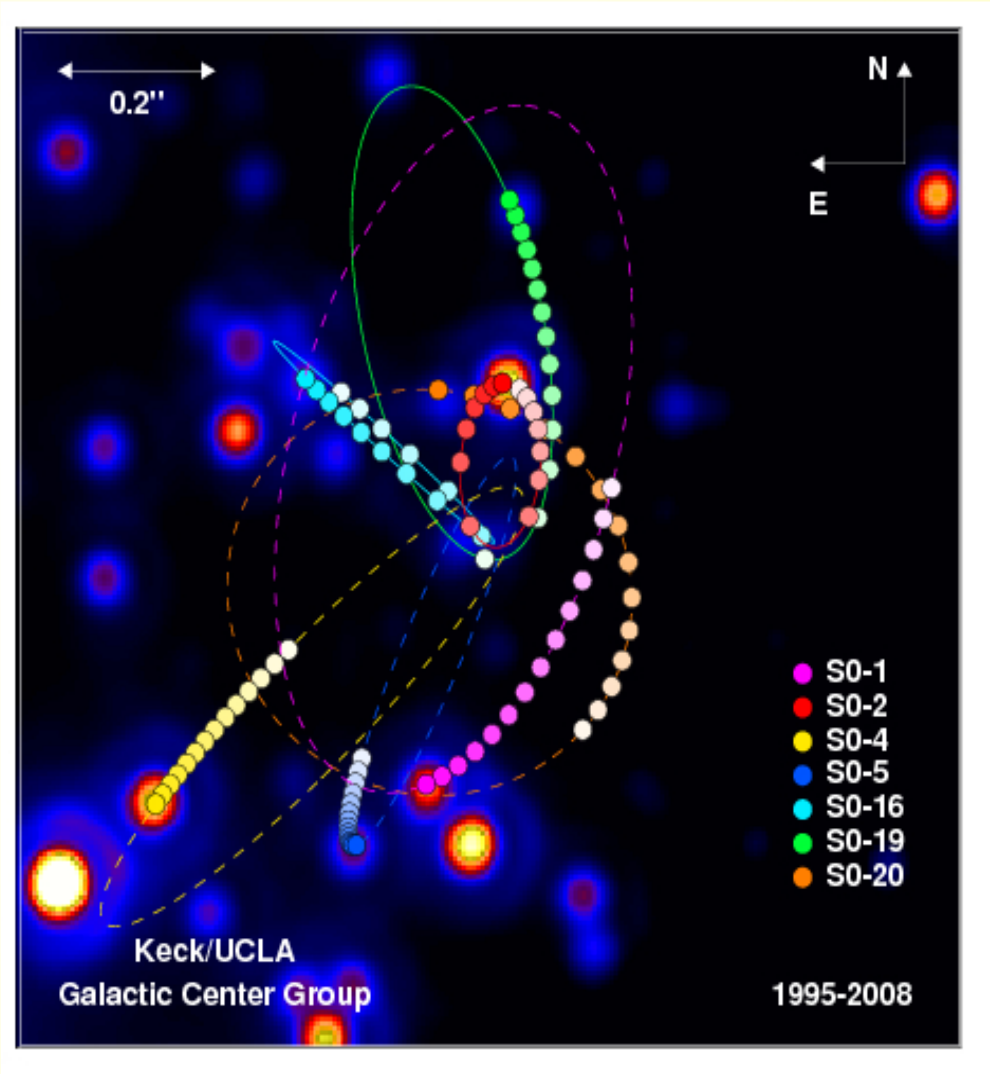

Sky map in SMBH-s

Supermassive black hole spin-flip during the inspiral
L. Á. Gergely, P. L. Biermann, L. I. Caramete, Class. Quantum Grav. **27** (2010) 194009

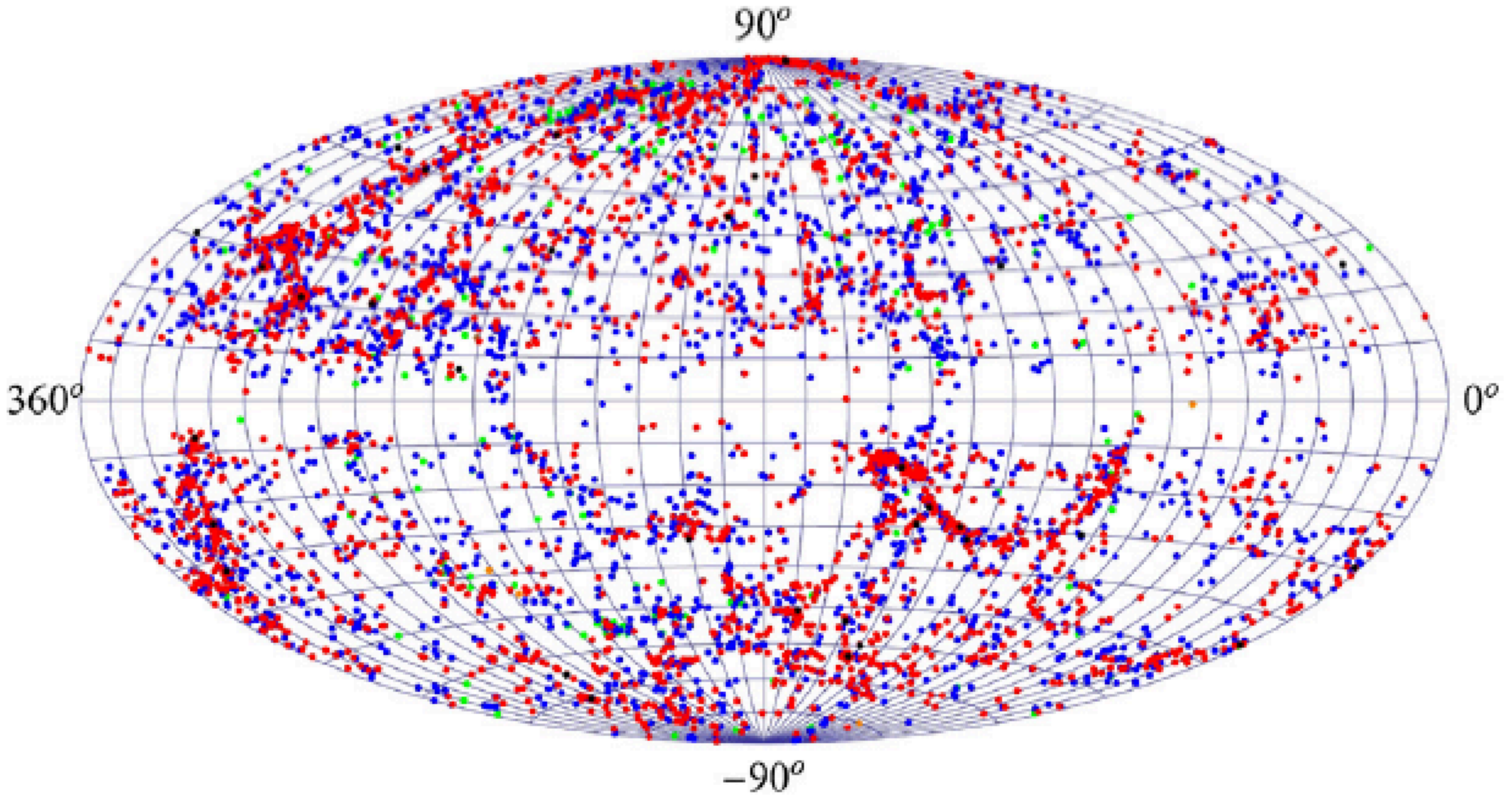

Figure 1. Aitoff projection in galactic coordinates of 5895 NED SMBH candidate sources. The sample is complete in a sensitivity sense; in order to derive densities one needs a volume correction. The color code (online only) is orange, green, blue, red, black corresponding to masses above $10^5\,M_\odot$, $10^6\,M_\odot$, $10^7\,M_\odot$, $10^8\,M_\odot$, $10^9\,M_\odot$, respectively. With the exception of the less numerous first range (orange), representing compact star clusters, the rest are SMBHs.

Photon ring of the SMBH Pōwehi in M87 – Event Horizon Telescope

THE ASTROPHYSICAL JOURNAL LETTERS

Table of contents

Volume 875
Number 1, 2019 April 10

‹ Previous issue

View all abstracts

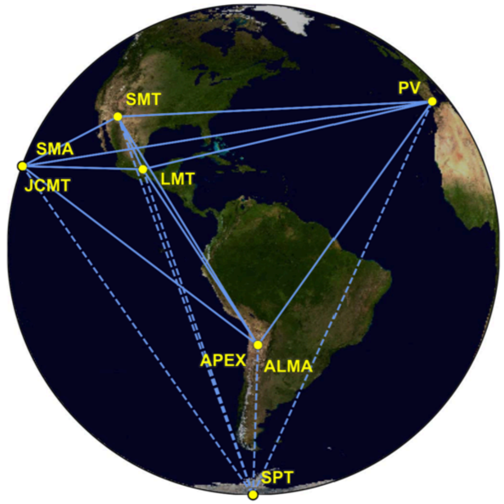

Figure 1. Eight stations of the EHT 2017 campaign over six geographic locations as viewed from the equatorial plane. Solid baselines represent mutual visibility on M87* (+12° declination). The dashed baselines were used for the calibration source 3C279 (see Papers III and IV).

The Universe under the Microscope – Astrophysics at High Angular Resolution IOP Publishing
Journal of Physics: Conference Series **131** (2008) 012053 doi:10.1088/1742-6596/131/1/012053

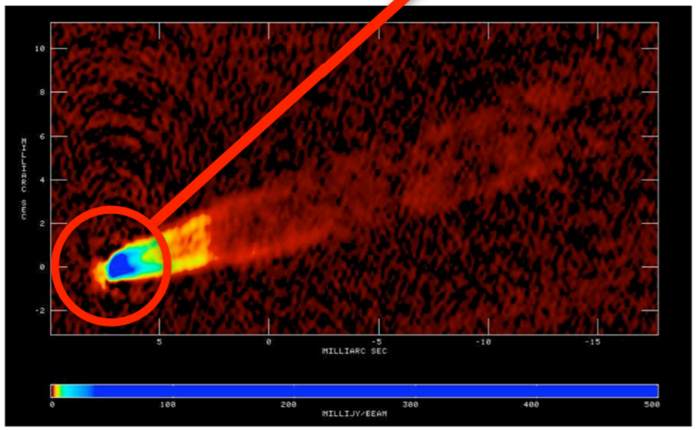

Figure 2. A composite VLBA image of M87 at 43 GHz made by summing the images from the first 9 epochs of the movie project. The resolution is 0.43 × 0.21 mas elongated along position angle −16°. The image peak is 643 mJy beam^{-1} and the off-source rms is 0.18 mJy beam^{-1}. Because this image is the sum of several images made at different times, individual features will be blurred out and the jet will appear smoother than it actually is, much like what is seen in a long-exposure photograph of moving water.

The EHT Collaboration et al.

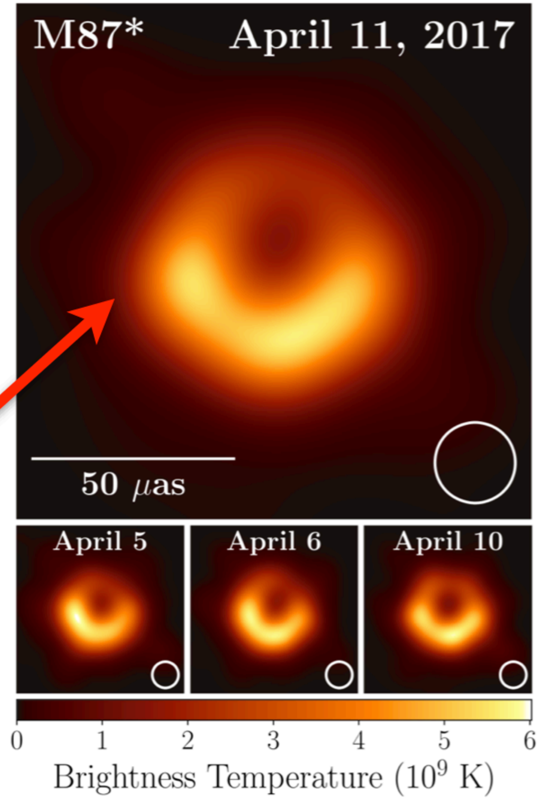

Figure 3. Top: EHT image of M87* from observations on 2017 April 11 as a representative example of the images collected in the 2017 campaign. The image is the average of three different imaging methods after convolving each with a circular Gaussian kernel to give matched resolutions. The largest of the three kernels (20 μas FWHM) is shown in the lower right. The image is shown in units of brightness temperature, $T_b = S\lambda^2/2k_B\Omega$, where S is the flux density, λ is the observing wavelength, k_B is the Boltzmann constant, and Ω is the solid angle of the resolution element. Bottom: similar images taken over different days showing the stability of the basic image structure and the equivalence among different days. North is up and east is to the left.

https://iopscience.iop.org/article/10.1088/1742-6596/131/1/012053/pdf?fbclid=IwAR258WA8ofbOCkeFwO3HuaD9yZQ0V4FNE9MGCsmj1r_y229EuuqgtJnbNul

Indirect proof of gravitational waves: the Hulse-Taylor pulsar

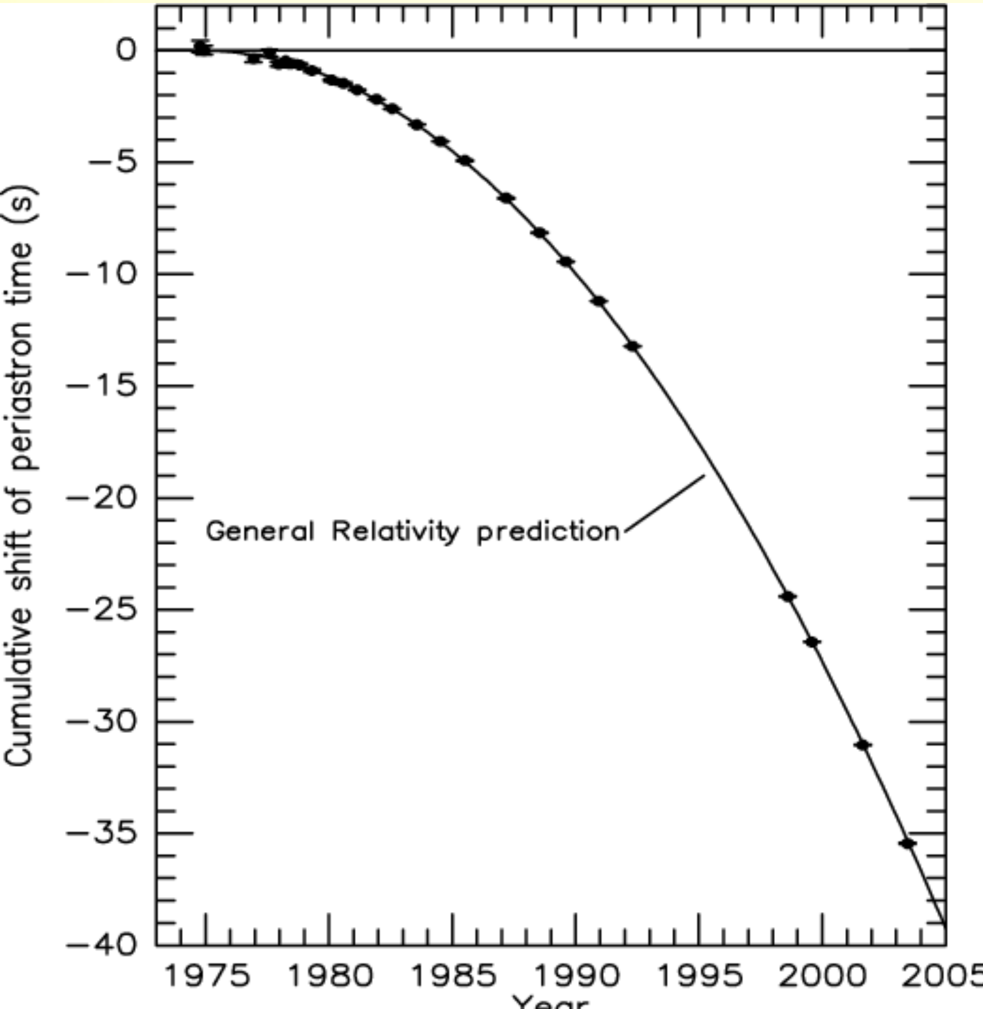

40s change in 30 years!! $(4x10^{-8})$

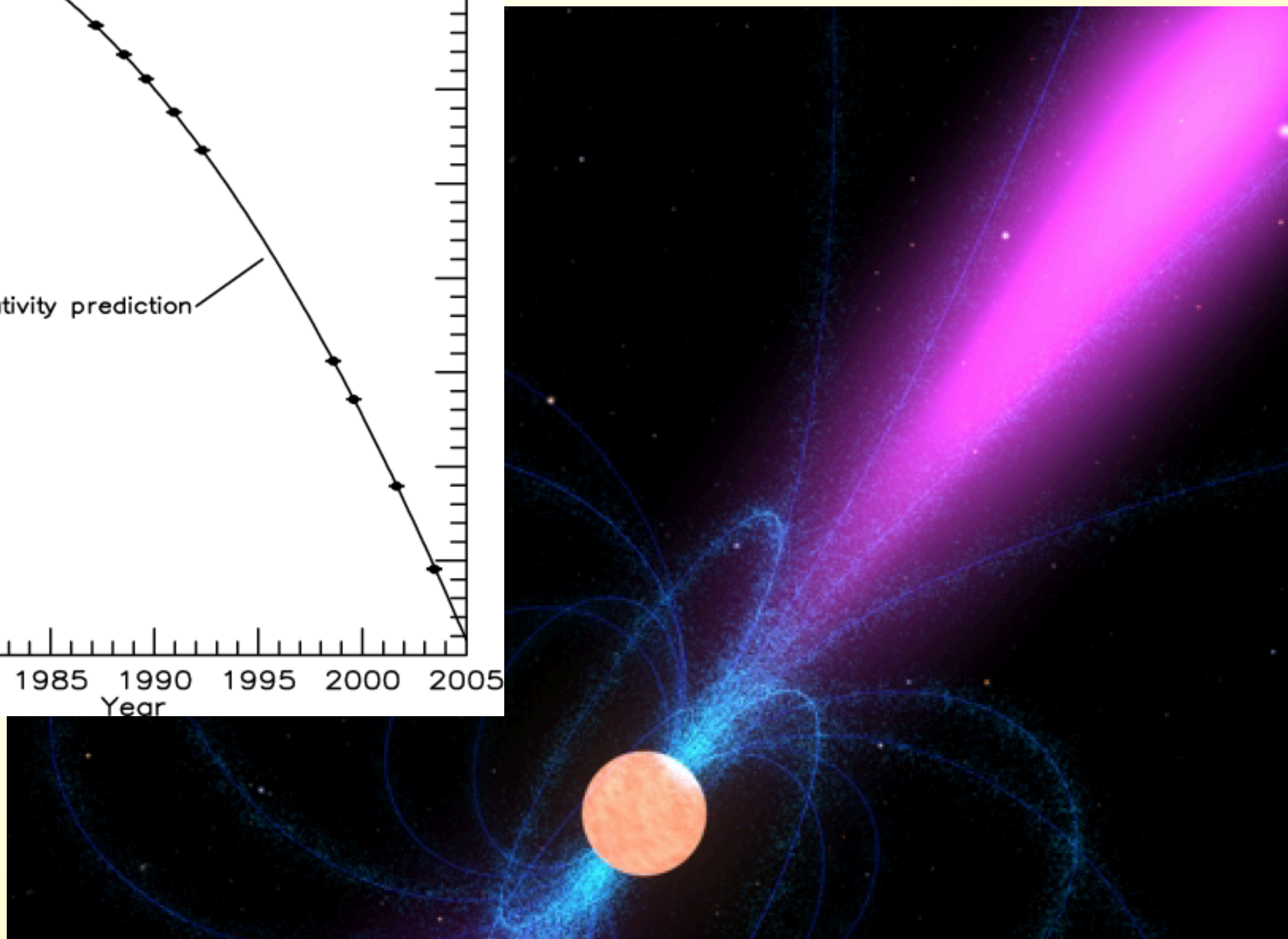

Nobel-prize
1993

The LIGO Scientific Collaboration

LIGO Scientific Collaboration

Abilene Christian University
Albert-Einstein Institut
American University
Andrews University
Bellevue College
California Institute of Technology
California State Univ., Fullerton
California State Univ., Los Angeles
Canadian Inst. Th. Astrophysics
Carleton College
Chinese University of Hong Kong
College of William and Mary
Colorado State University
Columbia U. in the City of New York
Cornell University
Embry-Riddle Aeronautical Univ.
Eötvös Loránd University
Georgia Institute of Technology
Goddard Space Flight Center
GW-INPE, Sao Jose Brasil
Hillsdale College
Hobart & William Smith Colleges
IAP – Nizhny Novogorod
IIP-UFRN
IndIGO
Kenyon College
Korean Gravitational-Wave Group
Louisiana State University
Marshall Space Flight Center
Montana State University
Montclair State University
Moscow State University
National Tsing Hua University
NCSARG – Univ. of Illinois, Urbana-Champaign
Northwestern University
Penn State University
Rochester Institute of Technology
Sonoma State University
Southern University
Stanford University
Syracuse University
Texas Tech University
Trinity University
Tsinghua University
U. Montreal / Polytechnique
University of Brussels
University of Chicago
University of Florida
University of Maryland
University of Michigan
University of Minnesota
University of Mississippi
University of Oregon
University of Sannio
University of Szeged
University of Texas Rio Grande
University of the Balearic Islands
University of Tokyo
University of Washington
University of Washington Bothell
University of Wisconsin – Milwaukee
USC – Information Sciences Institute
Washington State University – Pullman
West Virginia University
Whitman College

LIGO Laboratory: California Institute of Technology, Massachusetts Institute of Technology, LIGO Hanford Observatory, LIGO Livingston Observatory

Australian Consortium for Interferometric Gravitational Astronomy (ACIGA):
Australian National University, Charles Sturt University, Monash University, Swinburne University, University of Adelaide, University of Melbourne, University of Western Australia

German/British Collaboration for the Detection of Gravitational Waves (GEO600):
Albert-Einstein Institut, Hannover, Cardiff University, King's College University of London, Leibniz Universität Hannover, University of Birmingham, University of Cambridge, University of Glasgow, University of Hamburg, University of Sheffield, University of Southampton, University of Strathclyde, University of the West of Scotland, University of Zurich

First direct detection of GWs: GW150914

Phys. Rev. Lett.
116, 061102 (2016)

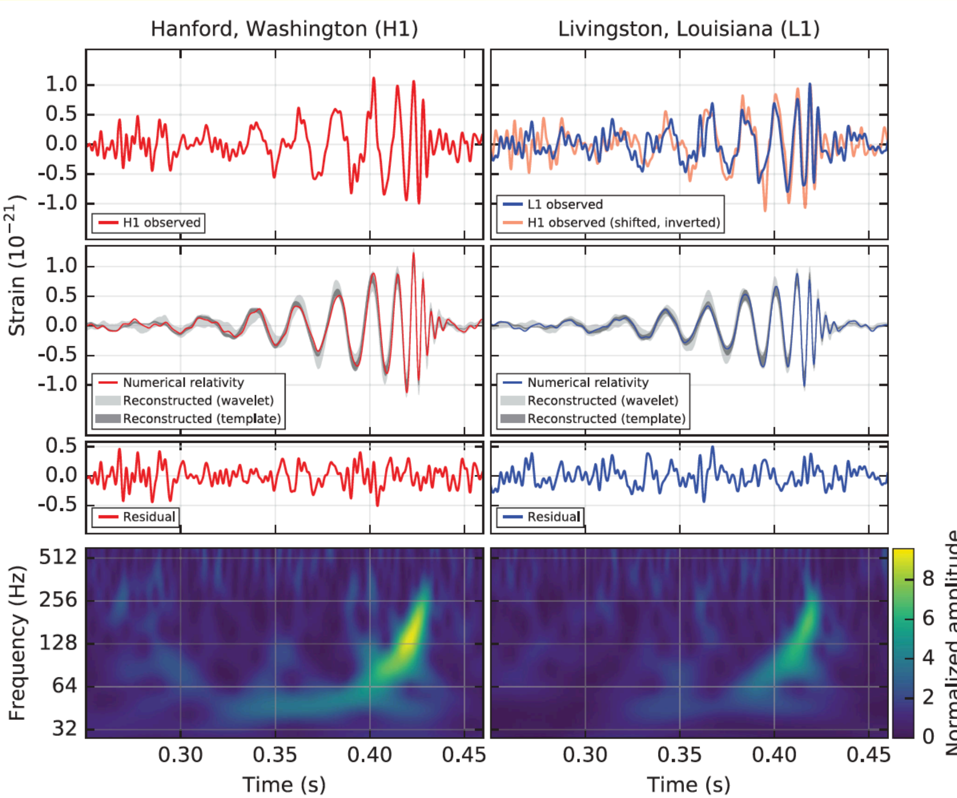

GW150914:FACTSHEET

BACKGROUND IMAGES: TIME-FREQUENCY TRACE (TOP) AND TIME-SERIES (BOTTOM) IN THE TWO LIGO DETECTORS; SIMULATION OF BLACK HOLE HORIZONS (MIDDLE-TOP), BEST FIT WAVEFORM (MIDDLE-BOTTOM)

first direct detection of gravitational waves (GW) and first direct observation of a black hole binary

observed by	LIGO L1, H1
source type	black hole (BH) binary
date	14 Sept 2015
time	09:50:45 UTC
likely distance	0.75 to 1.9 Gly 230 to 570 Mpc
redshift	0.054 to 0.136
signal-to-noise ratio	24
false alarm prob.	< 1 in 5 million
false alarm rate	< 1 in 200,000 yr
Source Masses	M⊙
total mass	60 to 70
primary BH	32 to 41
secondary BH	25 to 33
remnant BH	58 to 67
mass ratio	0.6 to 1
primary BH spin	< 0.7
secondary BH spin	< 0.9
remnant BH spin	0.57 to 0.72
signal arrival time delay	arrived in L1 7 ms before H1
likely sky position	Southern Hemisphere
likely orientation	face-on/off
resolved to	~600 sq. deg.

duration from 30 Hz	~ 200 ms
# cycles from 30 Hz	~10
peak GW strain	1×10^{-21}
peak displacement of interferometers arms	±0.002 fm
frequency/wavelength at peak GW strain	150 Hz, 2000 km
peak speed of BHs	~ 0.6 c
peak GW luminosity	3.6×10^{56} erg s^{-1}
radiated GW energy	2.5-3.5 M⊙
remnant ringdown freq.	~ 250 Hz
remnant damping time	~ 4 ms
remnant size, area	180 km, 3.5×10^5 km^2
consistent with general relativity?	passes all tests performed
graviton mass bound	< 1.2×10^{-22} eV
coalescence rate of binary black holes	2 to 400 Gpc^{-3} yr^{-1}
online trigger latency	~ 3 min
# offline analysis pipelines	5
CPU hours consumed	~ 50 million (=20,000 PCs run for 100 days)
papers on Feb 11, 2016	13
# researchers	~1000, 80 institutions in 15 countries

Detector noise introduces errors in measurement. Parameter ranges correspond to 90% credible bounds.
Acronyms: L1=LIGO Livingston, H1=LIGO Hanford; Gly=giga lightyear=9.46×10^{12} km; Mpc=mega parsec=3.2 million lightyear, Gpc=10^3 Mpc, fm=femtometer=10^{-15} m, M⊙=1 solar mass=2×10^{30} kg

First direct detection of GWs: GW150914

Phys. Rev. Lett. **116**, 061102 (2016)

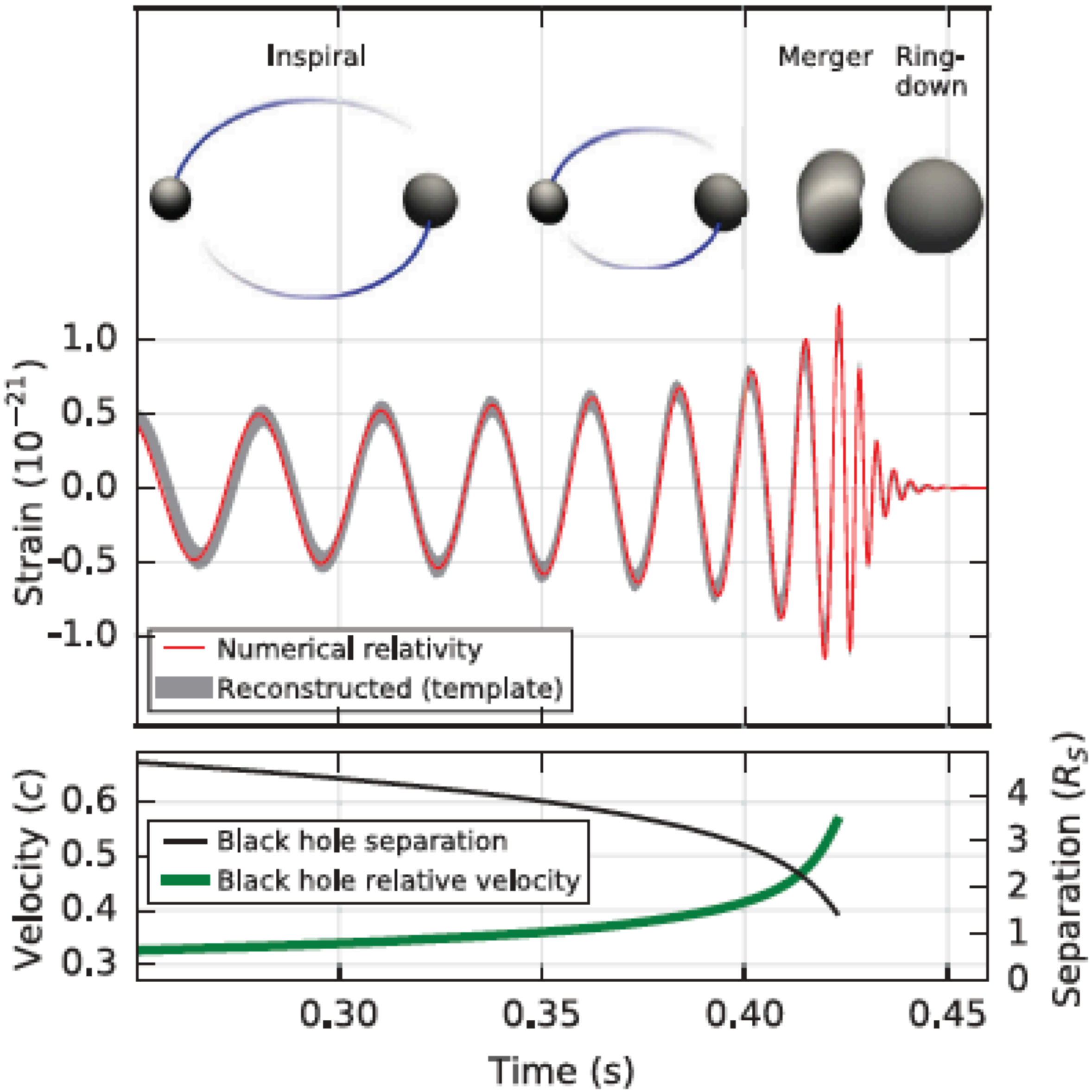

BHs of 29 and 36 solar masses merge →
In only 0.05 sec energy corresponding to 3 solar masses is produced in the form of GWs = 10^{31} years of energy production of the Paks Nuclear Plant!

Due to the large distance in the laser interferometers of Advanced LIGO it produced one part in one thousand change of the proton radius !

Where was GW150914 coming from? (230-500 Mpc)

Milky Way ~ 30 kpc

Laniakea supercluster ~ 160 Mpc

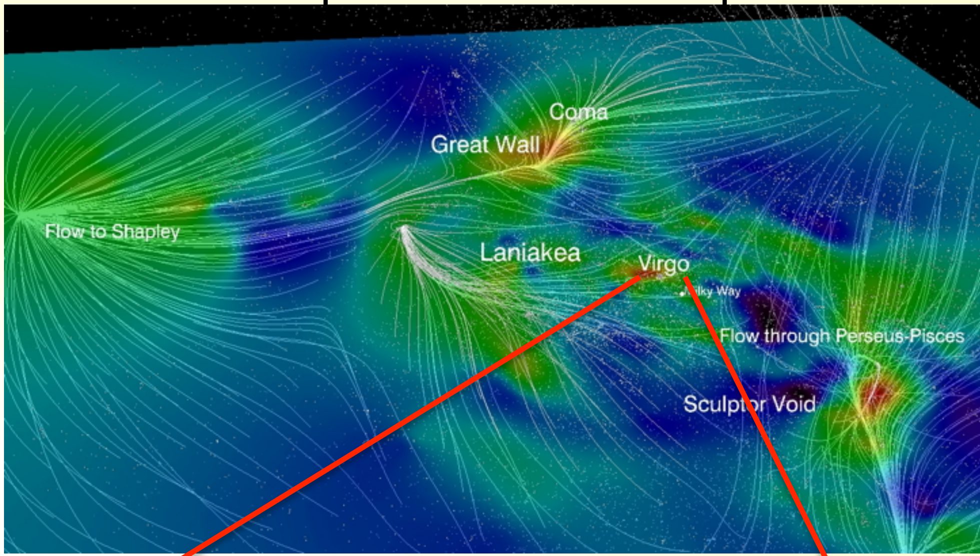

Local Group ~ 3,1 Mpc

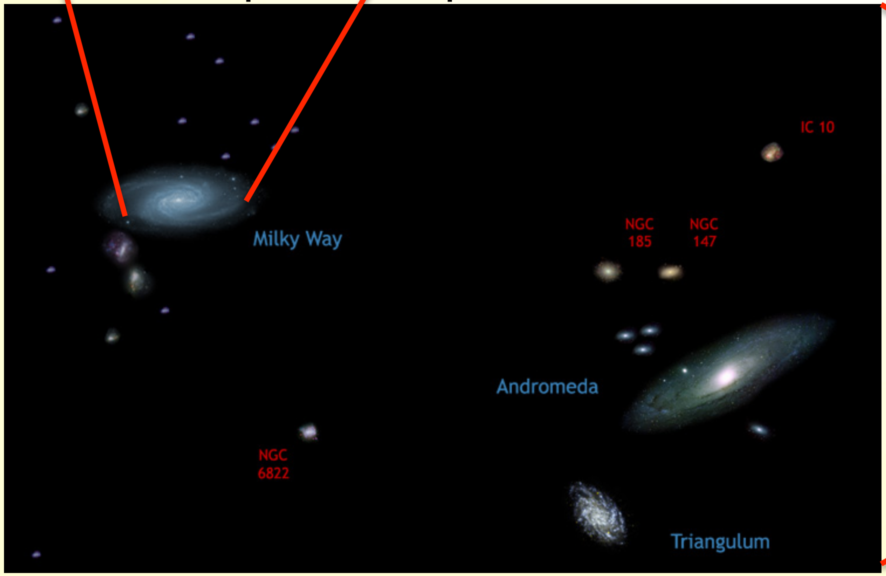

Virgo supergroup ~ 33 Mpc

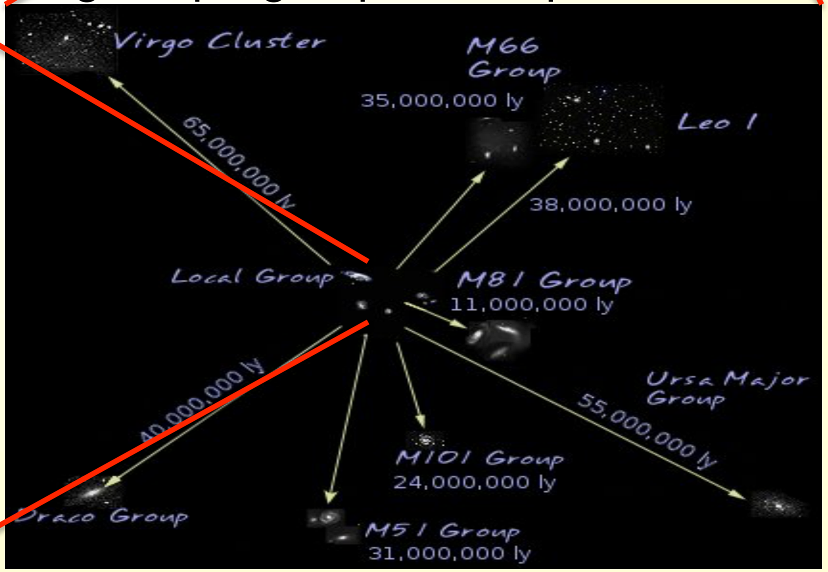

Where was GW150914 coming from? (230-500 Mpc)

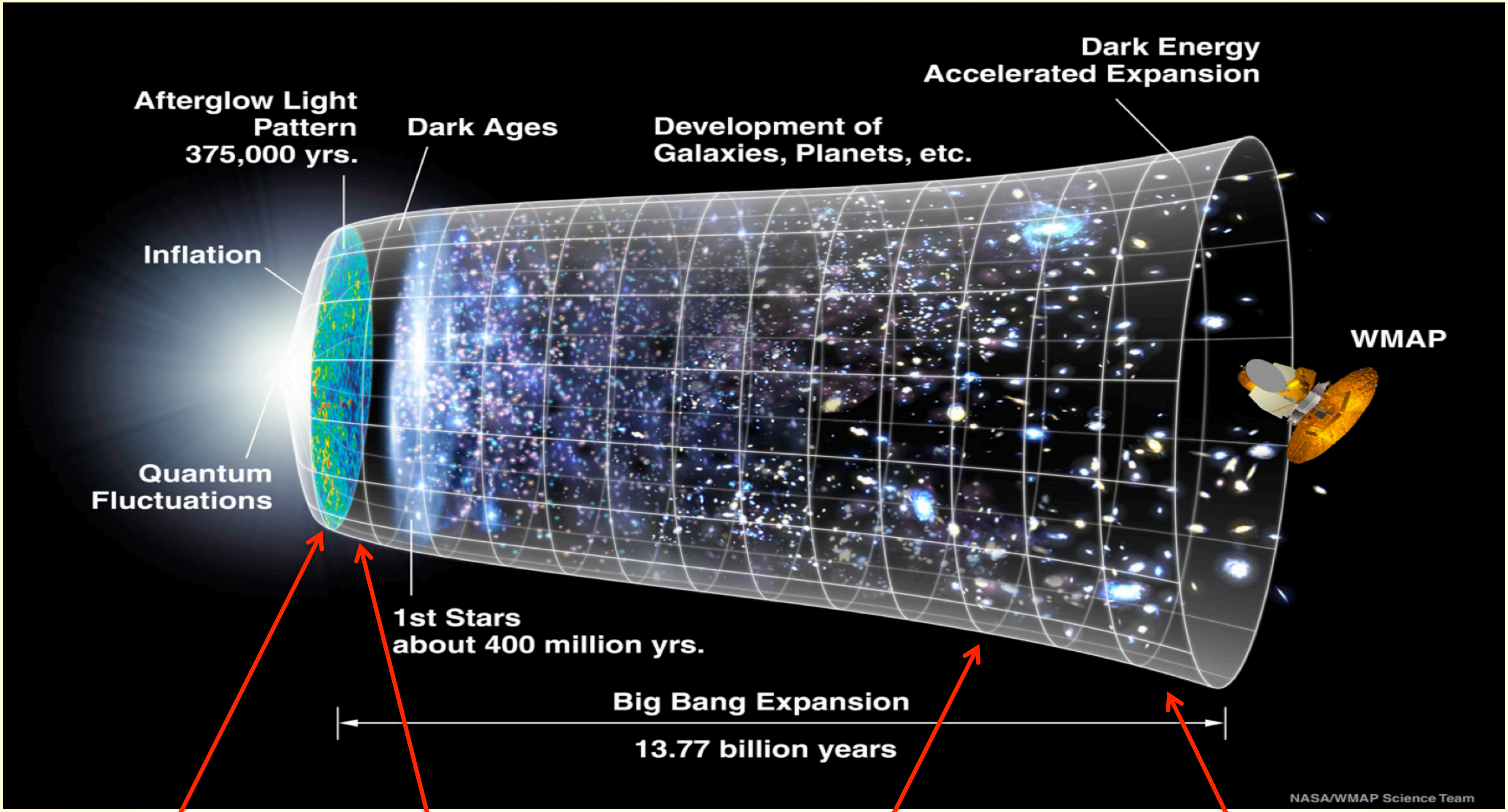

Big Bang
(13.7 billion ys)

Dark Ages
no light,
but GWs!!

accelerated expansion
starts

GW150914
~ z=0.1 (1.3 billion ys)
Oxigen filled atmosphere

Network of second generation gravitational wave observatories

Advanced LIGO, Hanford, USA, 4km

Advanced LIGO, Livingston, USA, 4km

Advanced Virgo, Cascina, Italy, 3km

KAGRA, Kamioke, Japan, 3km

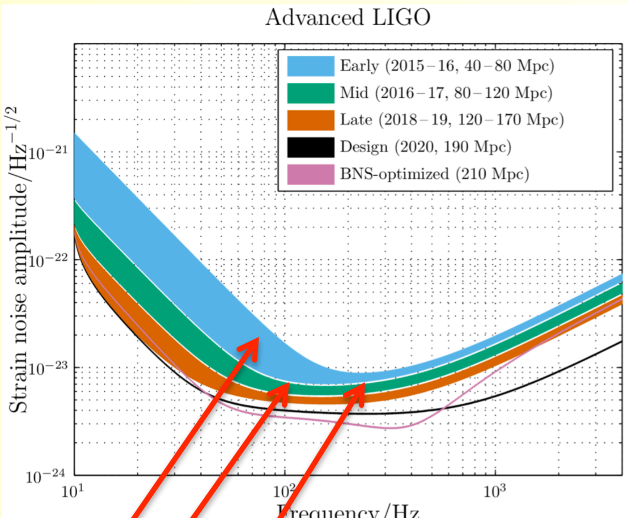

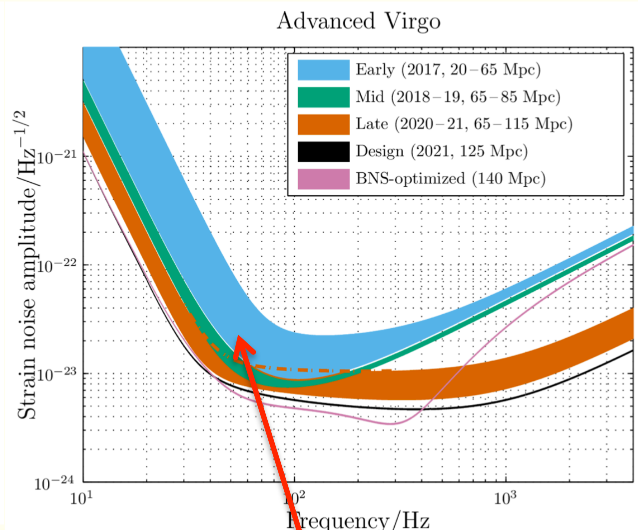

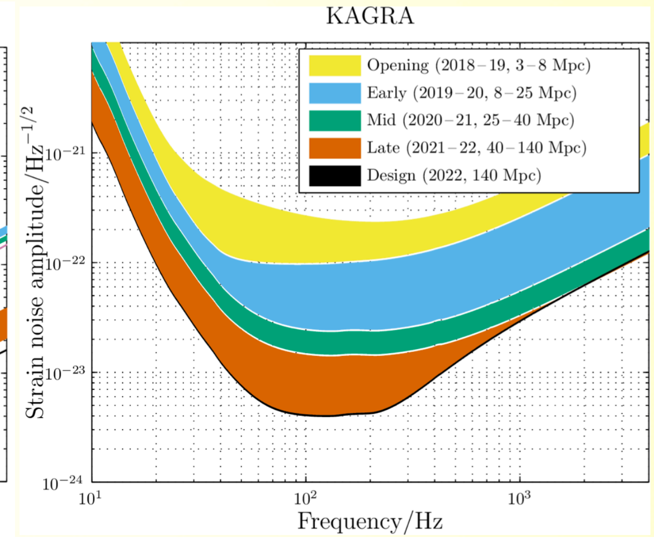

GW150915 GW151012 GW151226 O1

GW170104 GW170608 GW170729 O2

GW170809 GW170814 GW170817 O2
GW170818 GW170823

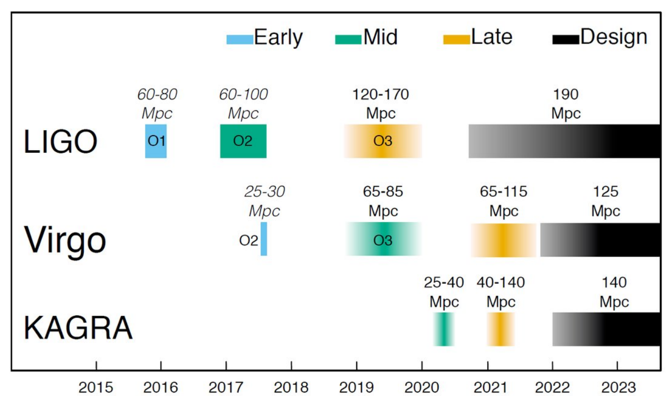

Gravitational waves from BH coalescence in O1 and O2

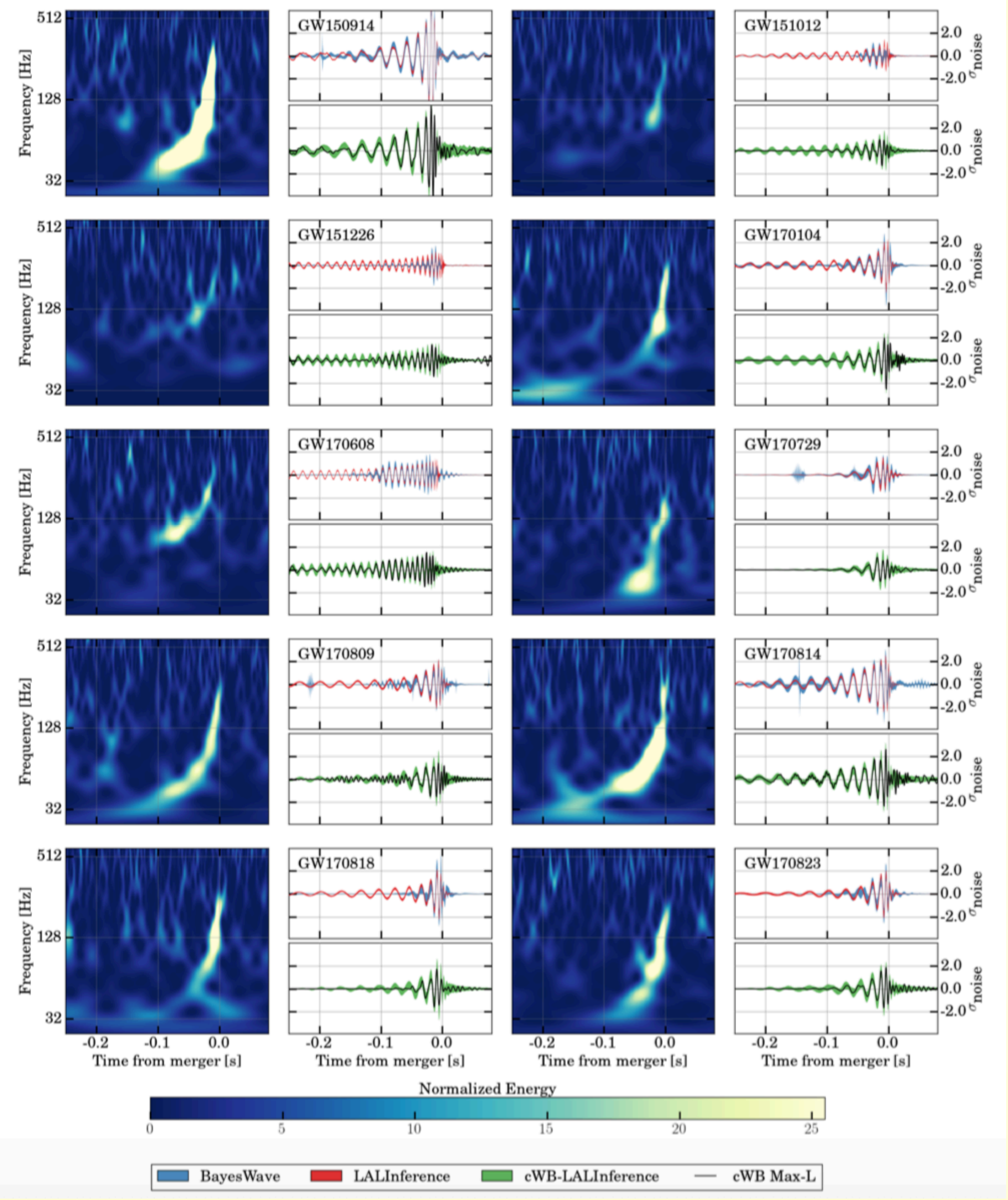

Gravitational waves in O3

GraceDB — Gravitational-Wave Candidate Event Database

HOME | PUBLIC ALERTS | SEARCH | LATEST | DOCUMENTATION | LOGIN

Latest — as of 30 September 2019 19:34:15 UTC

Test and MDC events and superevents are not included in the search results by default; see the query help for information on how to search for events and superevents in those categories.

Query:

Search for: Superevent

Search

UID	Labels	t_start	t_0	t_end	FAR (Hz)	UTC Created
S190930t	ADVOK EM_Selected SKYMAP_READY EMBRIGHT_READY PASTRO_READY DQOK GCN_PRELIM_SENT	1253889264.685342	1253889265.685342	1253889266.685342	1.543e-08	2019-09-30 14:34:30 UTC
S190930s	ADVOK EM_Selected SKYMAP_READY EMBRIGHT_READY PASTRO_READY DQOK GCN_PRELIM_SENT	1253885758.235347	1253885759.246810	1253885760.253734	3.008e-09	2019-09-30 13:36:04 UTC
S190928c	ADVNO EM_Selected SKYMAP_READY DQOK GCN_PRELIM_SENT	1253671923.328316	1253671923.364500	1253671923.400684	6.729e-09	2019-09-28 02:14:18 UTC
S190924h	PE_READY ADVOK EM_Selected SKYMAP_READY EMBRIGHT_READY PASTRO_READY DQOK GCN_PRELIM_SENT	1253326743.785645	1253326744.846654	1253326745.876674	8.928e-19	2019-09-24 02:19:25 UTC
S190923y	ADVOK EM_Selected SKYMAP_READY EMBRIGHT_READY PASTRO_READY DQOK GCN_PRELIM_SENT	1253278576.645077	1253278577.645508	1253278578.654868	4.783e-08	2019-09-23 12:56:22 UTC
S190915ak	PE_READY ADVOK SKYMAP_READY EMBRIGHT_READY PASTRO_READY DQOK GCN_PRELIM_SENT	1252627039.685111	1252627040.690891	1252627041.730049	9.735e-10	2019-09-15 23:57:25 UTC
S190910h	PE_READY ADVOK SKYMAP_READY EMBRIGHT_READY PASTRO_READY DQOK GCN_PRELIM_SENT	1252139415.544299	1252139416.544448	1252139417.544448	3.584e-08	2019-09-10 08:30:21 UTC
S190910d	PE_READY ADVOK SKYMAP_READY EMBRIGHT_READY PASTRO_READY DQOK GCN_PRELIM_SENT	1252113996.241211	1252113997.242676	1252113998.264918	3.717e-09	2019-09-10 01:26:35 UTC
S190901ap	PE_READY ADVOK SKYMAP_READY EMBRIGHT_READY PASTRO_READY DQOK GCN_PRELIM_SENT	1251415878.837767	1251415879.837767	1251415880.838844	7.027e-09	2019-09-01 23:31:24 UTC
S190829u	PE_READY ADVNO SKYMAP_READY EMBRIGHT_READY PASTRO_READY DQOK GCN_PRELIM_SENT	1251147973.281494	1251147974.283940	1251147975.283940	5.151e-09	2019-08-29 21:06:19 UTC
S190828l	PE_READY ADVOK SKYMAP_READY EMBRIGHT_READY PASTRO_READY DQOK GCN_PRELIM_SENT	1251010526.884921	1251010527.886557	1251010528.913573	4.629e-11	2019-08-28 06:55:26 UTC
S190828j	PE_READY ADVOK SKYMAP_READY EMBRIGHT_READY PASTRO_READY DQOK GCN_PRELIM_SENT	1251009262.739486	1251009263.756472	1251009264.796332	8.474e-22	2019-08-28 06:34:21 UTC
S190822c	ADVNO SKYMAP_READY EMBRIGHT_READY PASTRO_READY DQOK GCN_PRELIM_SENT	1250472616.589125	1250472617.589203	1250472618.589203	6.145e-18	2019-08-22 01:30:23 UTC
S190816i	PE_READY ADVNO SKYMAP_READY EMBRIGHT_READY PASTRO_READY DQOK GCN_PRELIM_SENT	1249995888.757789	1249995889.757789	1249995890.757789	1.436e-08	2019-08-16 13:05:12 UTC
S190814bv	PE_READY ADVOK SKYMAP_READY EMBRIGHT_READY PASTRO_READY DQOK GCN_PRELIM_SENT	1249852255.996787	1249852257.012957	1249852258.021731	2.033e-33	2019-08-14 21:11:18 UTC
S190808ae	ADVNO SKYMAP_READY EMBRIGHT_READY PASTRO_READY DQOK GCN_PRELIM_SENT	1249338098.496141	1249338099.496141	1249338100.496141	3.366e-08	2019-08-08 22:21:45 UTC
S190728q	PE_READY ADVOK SKYMAP_READY EMBRIGHT_READY PASTRO_READY DQOK GCN_PRELIM_SENT	1248331527.497344	1248331528.546797	1248331529.706055	2.527e-23	2019-07-28 06:45:27 UTC
S190727h	PE_READY ADVOK SKYMAP_READY EMBRIGHT_READY PASTRO_READY DQOK GCN_PRELIM_SENT	1248242630.976288	1248242631.985887	1248242633.180176	1.378e-10	2019-07-27 06:03:51 UTC
S190720a	PE_READY ADVOK SKYMAP_READY EMBRIGHT_READY PASTRO_READY DQOK GCN_PRELIM_SENT	1247616533.703127	1247616534.704102	1247616535.860840	3.801e-09	2019-07-20 00:08:53 UTC
S190718y	ADVOK SKYMAP_READY EMBRIGHT_READY PASTRO_READY DQOK GCN_PRELIM_SENT	1247495729.067865	1247495730.067865	1247495731.067865	3.648e-08	2019-07-18 14:35:34 UTC
S190707q	PE_READY ADVOK SKYMAP_READY EMBRIGHT_READY PASTRO_READY DQOK GCN_PRELIM_SENT	1246527223.118398	1246527224.181226	1246527225.284180	5.265e-12	2019-07-07 09:33:44 UTC
S190706ai	PE_READY ADVOK SKYMAP_READY EMBRIGHT_READY PASTRO_READY DQOK GCN_PRELIM_SENT	1246487218.321541	1246487219.344727	1246487220.585938	1.901e-09	2019-07-06 22:26:57 UTC
S190701ah	PE_READY ADVOK SKYMAP_READY EMBRIGHT_READY PASTRO_READY DQOK GCN_PRELIM_SENT	1246048403.576563	1246048404.577637	1246048405.814941	1.916e-08	2019-07-01 20:33:24 UTC
S190630ag	PE_READY ADVOK SKYMAP_READY EMBRIGHT_READY PASTRO_READY DQOK GCN_PRELIM_SENT	1245955942.175325	1245955943.179550	1245955944.183184	1.435e-13	2019-06-30 18:52:28 UTC
S190602aq	PE_READY ADVOK SKYMAP_READY EMBRIGHT_READY PASTRO_READY DQOK GCN_PRELIM_SENT	1243533584.081266	1243533585.089355	1243533586.346191	1.901e-09	2019-06-02 17:59:51 UTC
S190524q	ADVNO SKYMAP_READY EMBRIGHT_READY PASTRO_READY DQOK GCN_PRELIM_SENT	1242708743.678669	1242708744.678669	1242708746.133301	6.971e-09	2019-05-24 04:52:30 UTC
S190521r	PE_READY ADVOK SKYMAP_READY EMBRIGHT_READY PASTRO_READY DQOK GCN_PRELIM_SENT	1242459856.453418	1242459857.460739	1242459858.642090	3.168e-10	2019-05-21 07:44:22 UTC
S190521g	PE_READY ADVOK SKYMAP_READY EMBRIGHT_READY PASTRO_READY DQOK GCN_PRELIM_SENT	1242442966.447266	1242442967.606934	1242442968.888184	3.801e-09	2019-05-21 03:02:49 UTC
S190519bj	PE_READY ADVOK SKYMAP_READY EMBRIGHT_READY PASTRO_READY DQOK GCN_PRELIM_SENT	1242315361.378873	1242315362.655762	1242315363.676270	5.702e-09	2019-05-19 15:36:04 UTC
S190518bb	ADVNO SKYMAP_READY EMBRIGHT_READY PASTRO_READY DQOK GCN_PRELIM_SENT	1242242376.474609	1242242377.474609	1242242380.922655	1.004e-08	2019-05-18 19:19:39 UTC
S190517h	PE_READY ADVOK SKYMAP_READY EMBRIGHT_READY PASTRO_READY DQOK GCN_PRELIM_SENT	1242107478.819517	1242107479.994141	1242107480.994141	2.373e-09	2019-05-17 05:51:23 UTC
S190513bm	PE_READY ADVOK SKYMAP_READY EMBRIGHT_READY PASTRO_READY DQOK GCN_PRELIM_SENT	1241816085.736106	1241816086.869141	1241816087.869141	3.734e-13	2019-05-13 20:54:48 UTC
S190512at	PE_READY ADVOK SKYMAP_READY EMBRIGHT_READY PASTRO_READY DQOK GCN_PRELIM_SENT	1241719651.411441	1241719652.416286	1241719653.518066	1.901e-09	2019-05-12 18:07:42 UTC
S190510g	ADVOK SKYMAP_READY EMBRIGHT_READY PASTRO_READY DQOK GCN_PRELIM_SENT	1241492396.291636	1241492397.291636	1241492398.293185	8.834e-09	2019-05-10 03:00:03 UTC
S190503bf	PE_READY ADVOK SKYMAP_READY EMBRIGHT_READY PASTRO_READY DQOK GCN_PRELIM_SENT	1240944861.288574	1240944862.412598	1240944863.422852	1.636e-09	2019-05-03 18:54:26 UTC
S190426c	PE_READY ADVOK SKYMAP_READY EMBRIGHT_READY PASTRO_READY DQOK GCN_PRELIM_SENT	1240327332.331668	1240327333.348145	1240327334.353516	1.947e-08	2019-04-26 15:22:15 UTC
S190425z	ADVOK SKYMAP_READY EMBRIGHT_READY PASTRO_READY DQOK	1240215502.011549	1240215503.011549	1240215504.018242	4.538e-13	2019-04-25 08:18:26 UTC
S190421ar	PE_READY ADVOK SKYMAP_READY EMBRIGHT_READY PASTRO_READY DQOK GCN_PRELIM_SENT	1239917953.250977	1239917954.409180	1239917955.409180	1.489e-08	2019-04-21 21:39:16 UTC
S190412m	PE_READY ADVOK SKYMAP_READY EMBRIGHT_READY PASTRO_READY DQOK GCN_PRELIM_SENT	1239082261.146717	1239082262.222168	1239082263.229492	1.683e-27	2019-04-12 05:31:03 UTC
S190408an	PE_READY ADVOK SKYMAP_READY EMBRIGHT_READY PASTRO_READY DQOK GCN_PRELIM_SENT	1238782699.268296	1238782700.287958	1238782701.359863	2.811e-18	2019-04-08 18:18:27 UTC
S190405ar	ADVNO SKYMAP_READY EMBRIGHT_READY PASTRO_READY DQOK	1238515307.863646	1238515308.863646	1238515309.863646	2.141e-04	2019-04-05 16:01:56 UTC

LIGO VIRGO LSC

Sky location of the sources (O1 & O2)

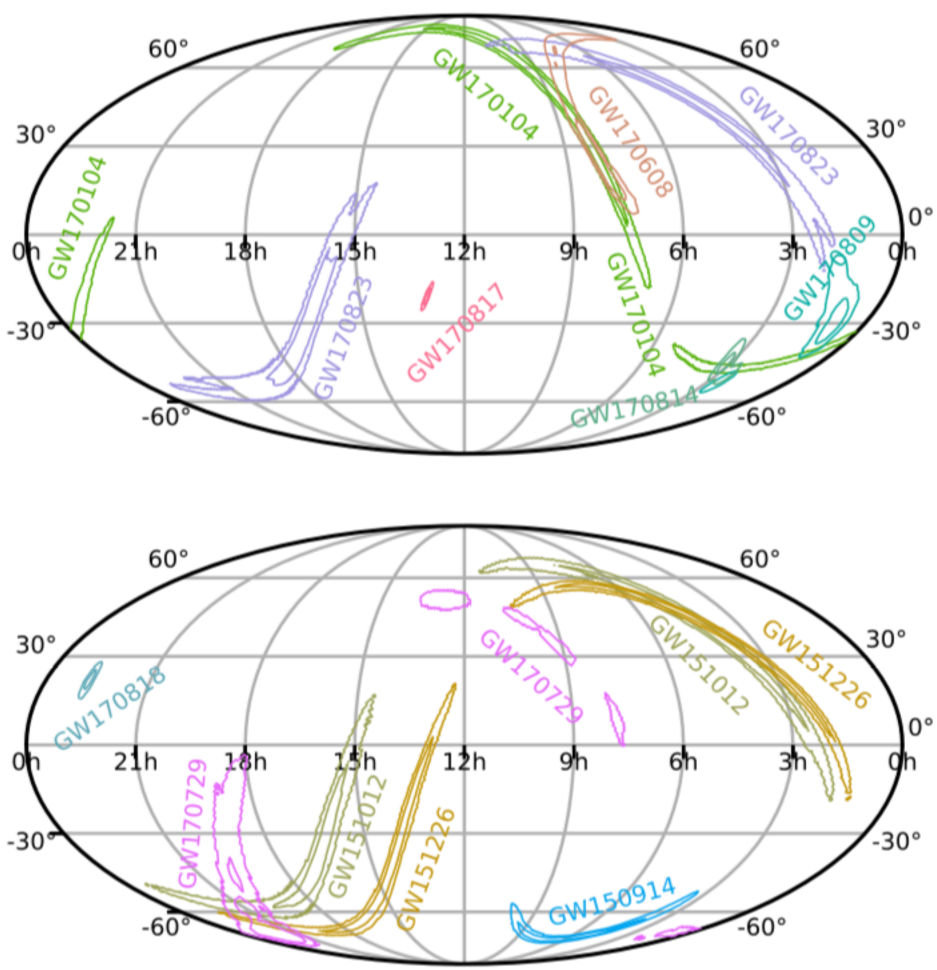

FIG. 8. Parameter estimation summary plots V. The contours show 90% and 50% credible regions for the sky locations of all GW events in a Mollweide projection. The probable position of the source is shown in equatorial coordinates (right ascension is measured in hours, and declination is measured in degrees). 50% and 90% credible regions of posterior probability sky areas for the GW events. *Top panel:* Confidently detected O2 GW events [22] (GW170817, GW170104, GW170823, GW170608, GW170809, GW170814) for which alerts were sent to EM observers. *Bottom panel:* O1 events (GW150914, GW151226, GW151012), along with O2 events (GW170729, GW170818) not previously released to EM observers.

The role of the third detector in localisation (GW170814)

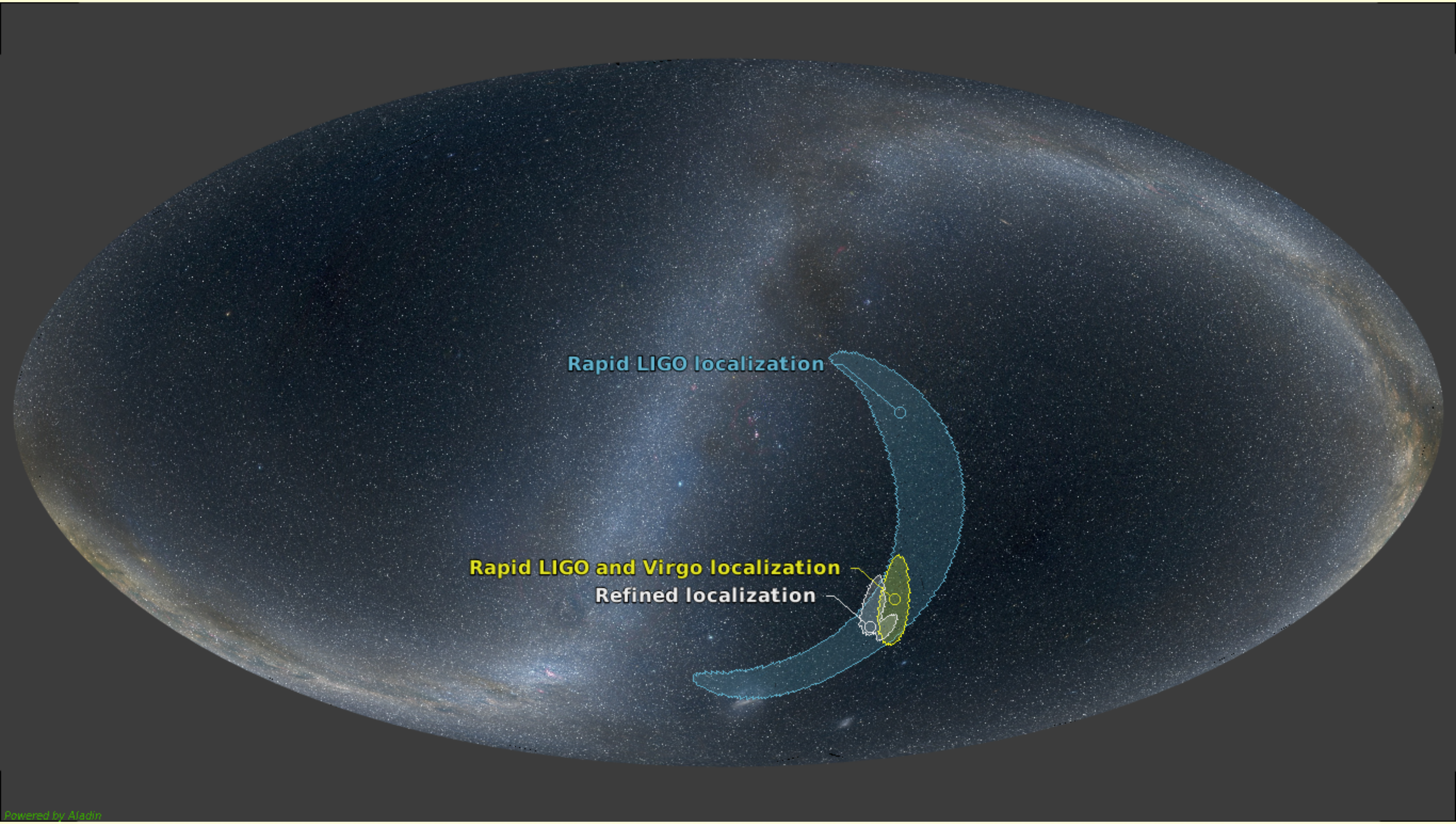

Mass ratio and spin estimates (O1 & O2)

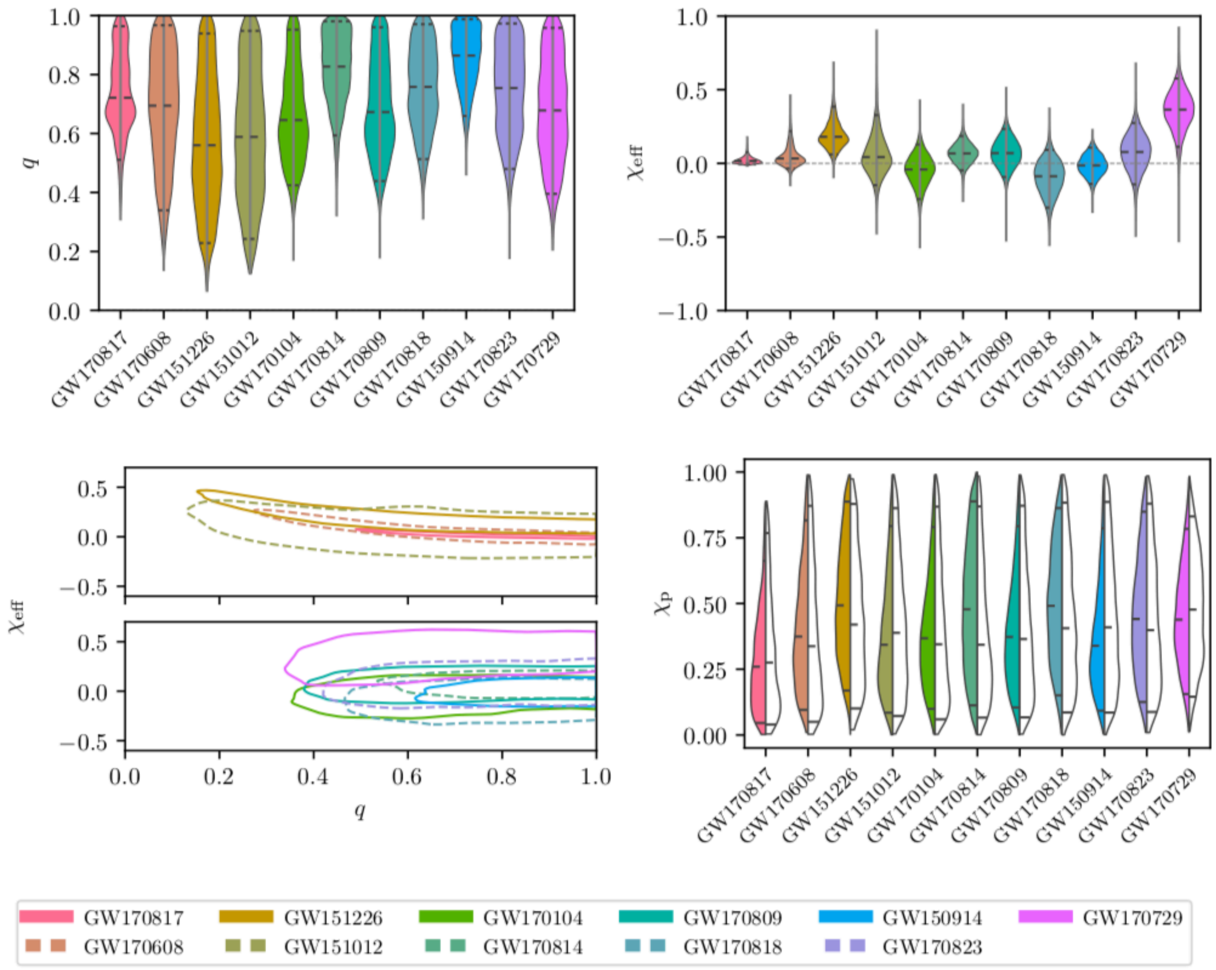

FIG. 5. Parameter estimation summary plots II. Posterior probability densities of the mass ratio and spin parameters of the GW events. The shaded probability distributions have equal maximum widths, and horizontal lines indicate the medians and 90% credible intervals of the distributions. For the two-dimensional distributions, the contours show 90% credible regions. Events are ordered by source frame chirp mass. The colors correspond to the colors used in summary plots. For GW170817 we show results for the high-spin prior $a_i < 0.89$. *Top left panel:* The mass ratio $q = m_2/m_1$. *Top right panel:* The effective aligned spin magnitude $\chi_{\rm eff}$. *Bottom left panel:* Contours of 90% credible regions for the effective aligned spin and mass ratio of the binary components for low (high) mass binaries are shown in the upper (lower) panel. *Bottom right panel:* The effective precession spin posterior (colored) and its effective prior distribution (white) for BBH (BNS) events. The priors have been conditioned on the $\chi_{\rm eff}$ posterior distributions.

Masses of the sources (O1 & O2)

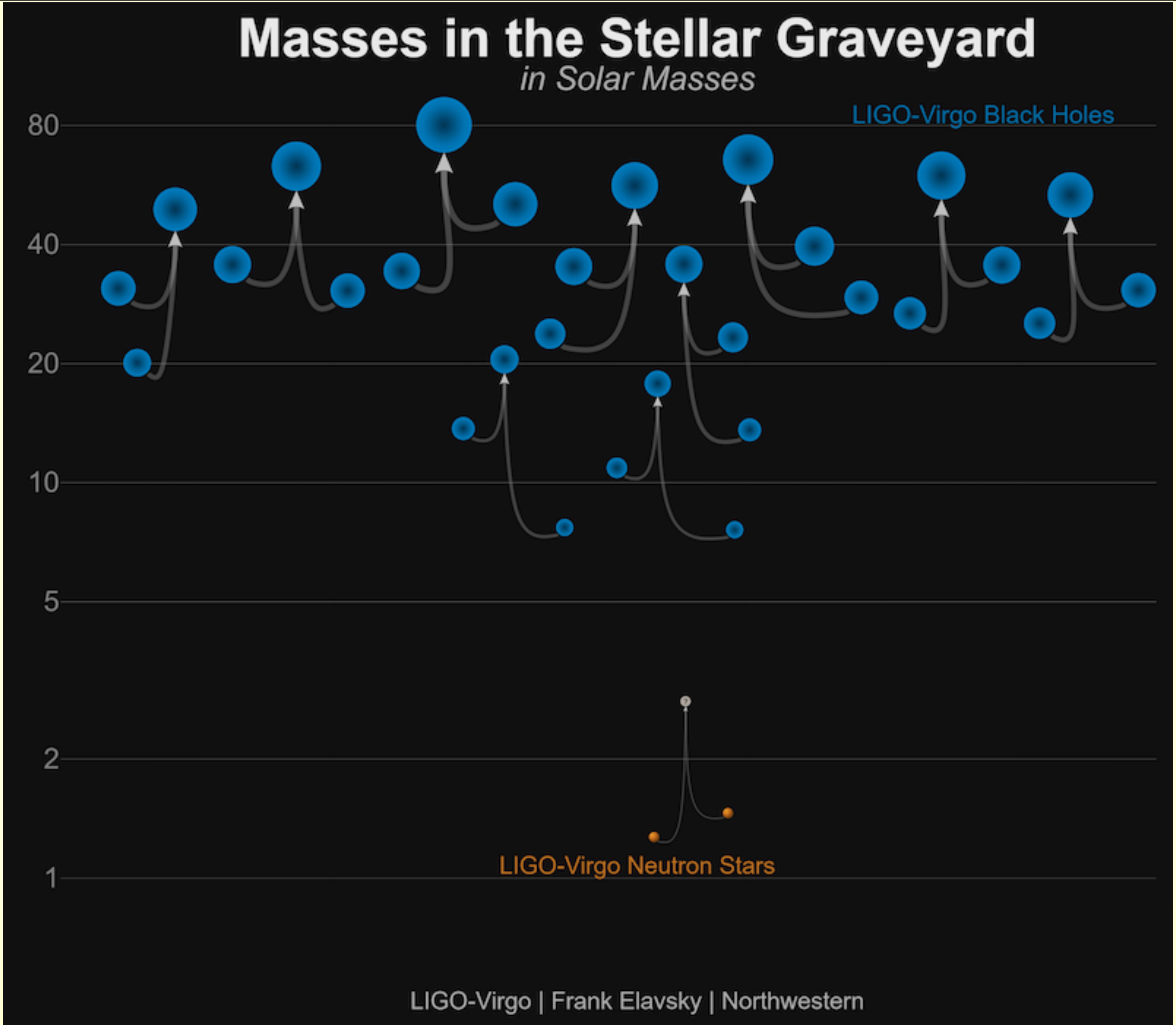

GW170817 and accompanying gamma-flare from a neutron-star binary merger

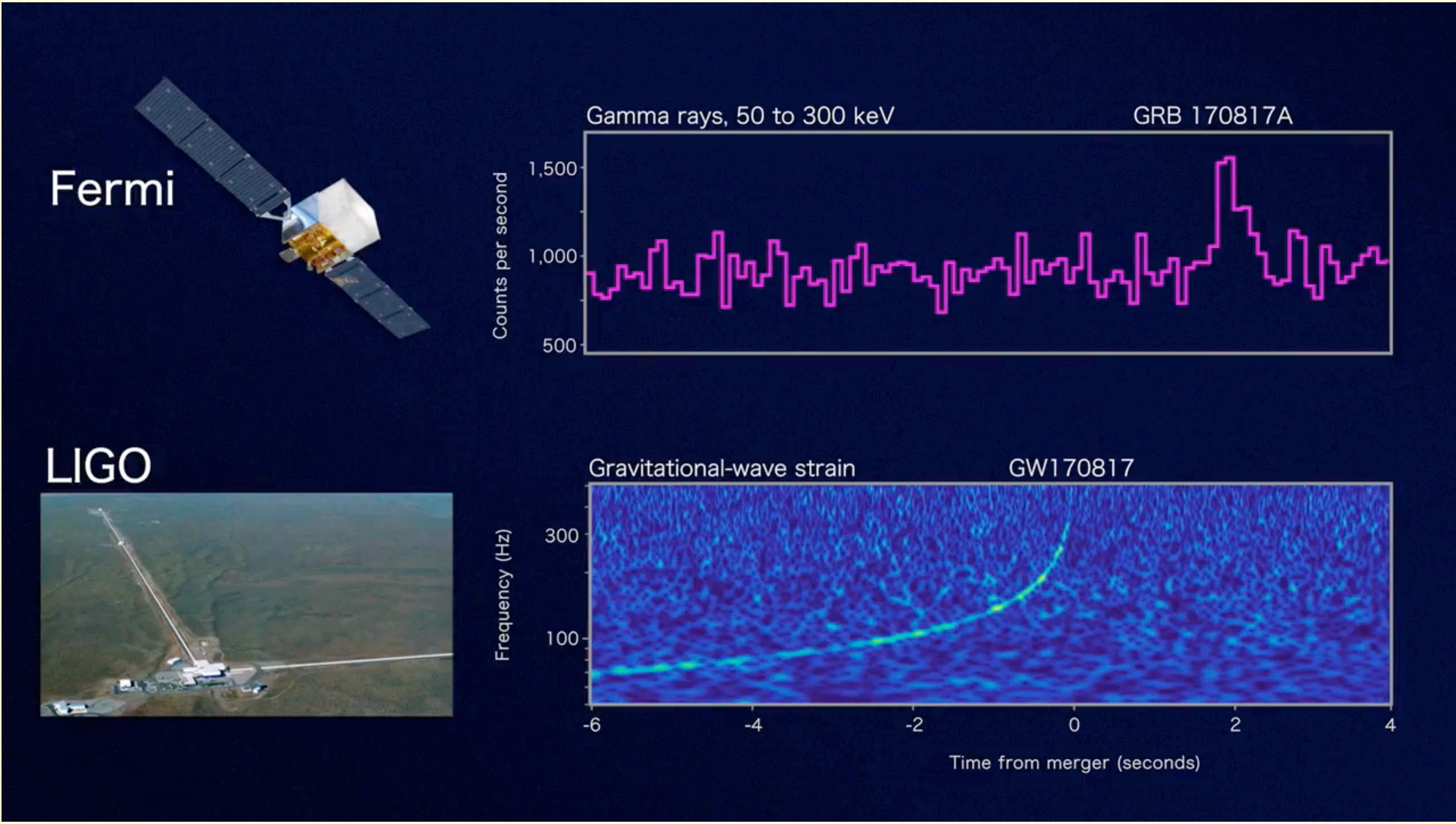

GW170817

Binary neutron star merger

A LIGO / Virgo gravitational wave detection with associated electromagnetic events observed by over 70 observatories.

H L V

Distance
130 million light years

Discovered
17 August 2017

Type
Neutron star merger

12:41:04 UTC
A gravitational wave from a binary neutron star merger is detected.

gravitational wave signal
Two neutron stars, each the size of a city but with the at least the mass of the sun, collided with each other.

gamma ray burst
A short gamma ray burst is an intense beam of gamma ray radiation which is produced just after the merger.

+ 2 seconds
A gamma ray burst is detected.

GW170817 allows us to measure the expansion rate of the universe directly using gravitational waves for the first time, and gives us a new way to infer its age

+10 hours 52 minutes
A new bright source of optical light is detected in a galaxy called NGC 4993, in the constellation of Hydra.

Detecting gravitational waves from a neutron star merger allows us to find out more about the structure of these unusual objects.

kilonova
Decaying neutron-rich material creates a glowing kilonova, producing heavy metals like gold and platinum.

+11 hours 36 minutes
Infrared emission observed.

+15 hours
Bright ultraviolet emission detected.

This multimessenger event provides confirmation that neutron star mergers can produce short gamma ray bursts.

+9 days
X-ray emission detected.

radio remnant
As material moves away from the merger it produces a shockwave in the interstellar medium - the tenuous material between stars. This produces emission which can last for years.

Au

The observation of a kilonova allowed us to show that neutron star mergers could be responsible for the production most of the heavy elements, like gold, in the universe.

+16 days
Radio emission detected.

Observing both electromagnetic and gravitational waves from the event provides compelling evidence that gravitational waves travel at the same speed as light.

GW170817 and accompanying electromagnetic detections

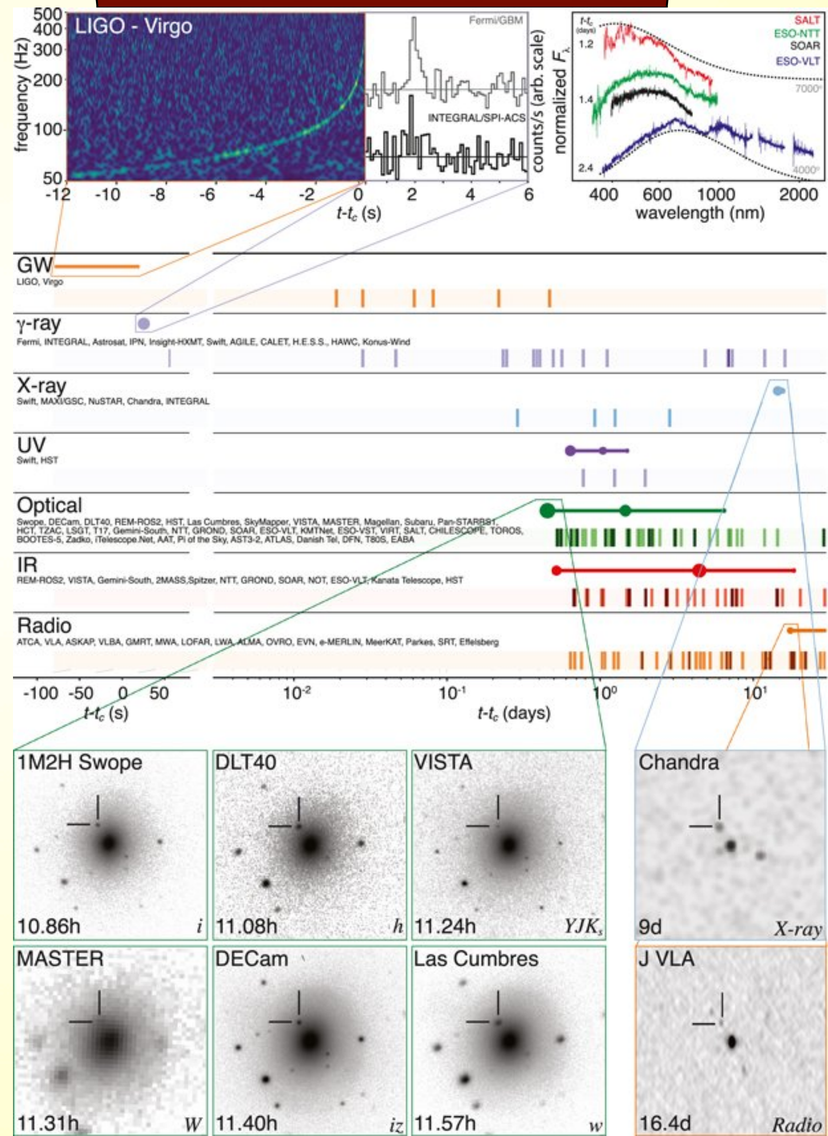

GW170817: production of heavy elements

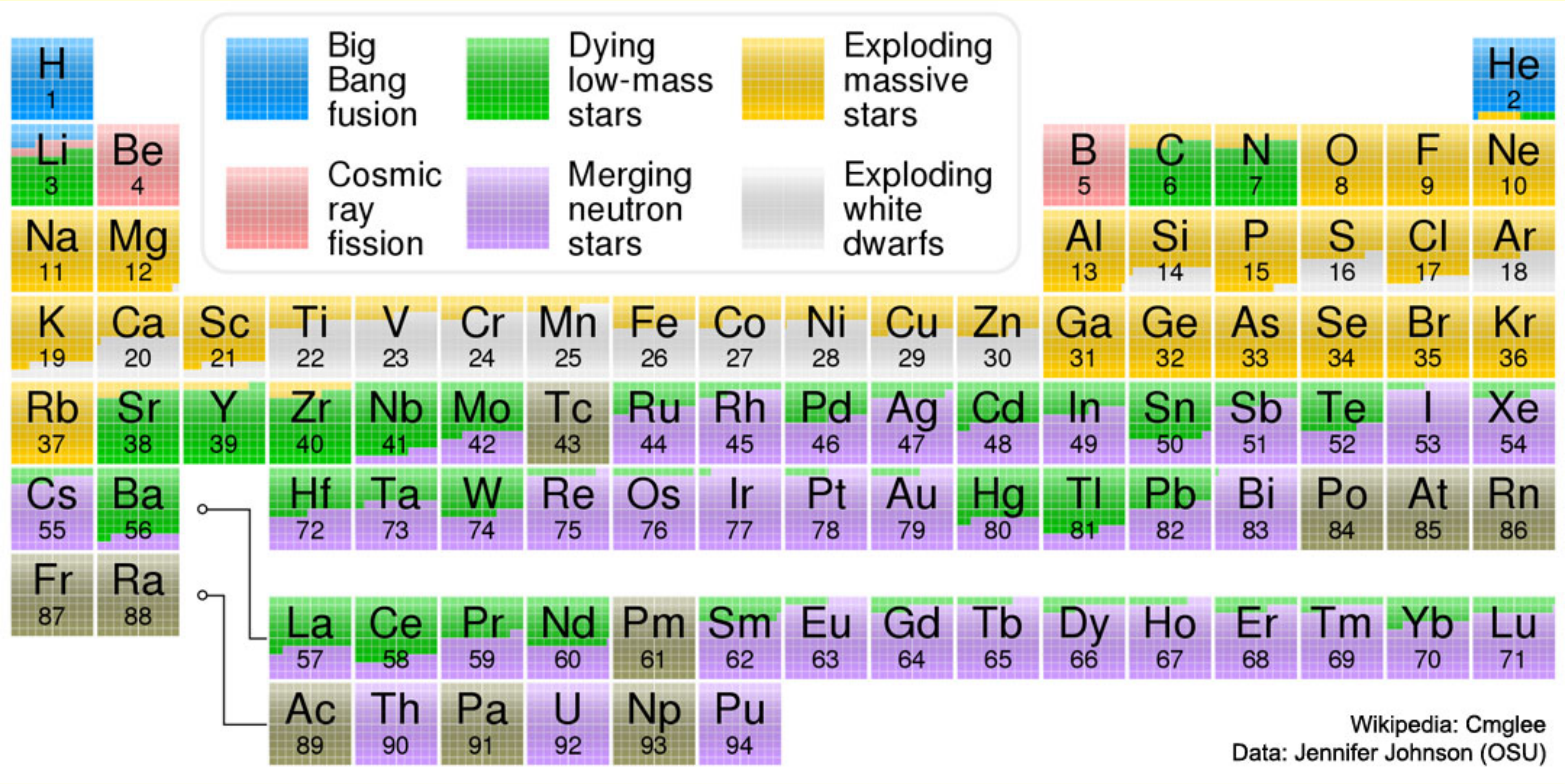

Cosmological consequences

RESEARCH LETTER

nature Accelerated Article Preview

LETTER
doi:10.1038/nature24471

A gravitational-wave standard siren measurement of the Hubble constant

The LIGO Scientific Collaboration and The Virgo Collaboration*, The 1M2H Collaboration*, The Dark Energy Camera GW-EM Collaboration and the DES Collaboration*, The DLT40 Collaboration*, The Las Cumbres Observatory Collaboration*, The VINROUGE Collaboration* & The MASTER Collaboration*

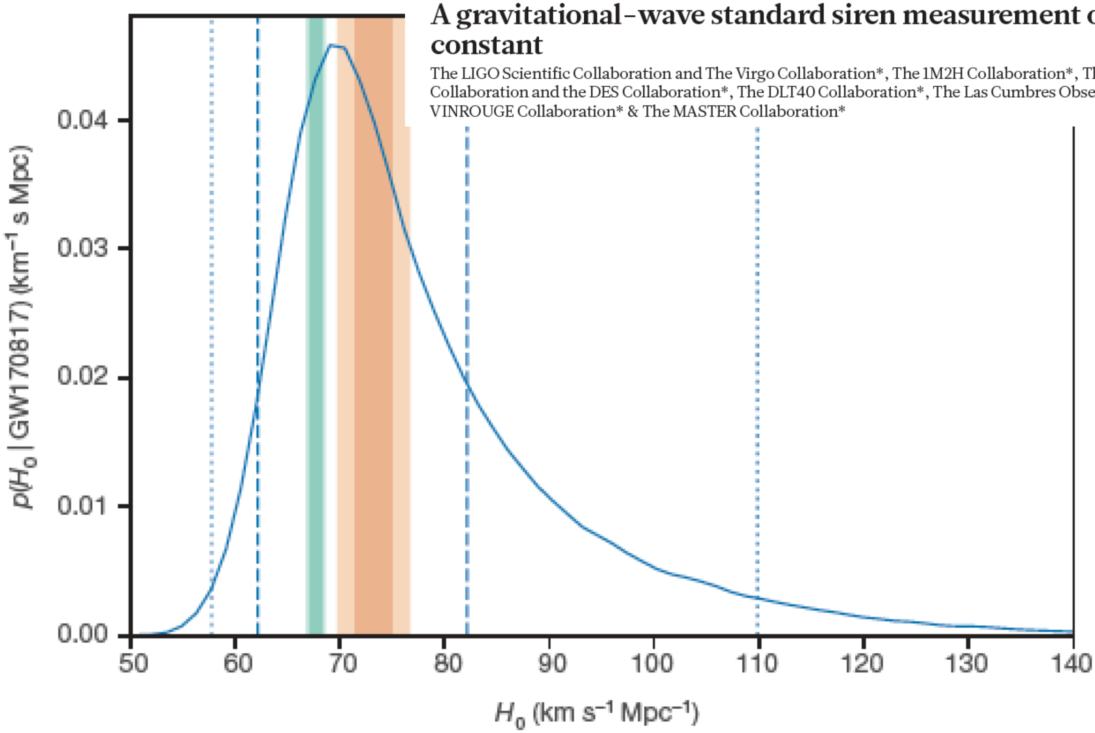

Figure 1 | GW170817 measurement of H_0. The marginalized posterior density for H_0, $p(H_0\,|\,\mathrm{GW170817})$, is shown by the blue curve. Constraints at 1σ (darker shading) and 2σ (lighter shading) from Planck[20] and SHoES[21] are shown in green and orange, respectively. The maximum a posteriori value and minimal 68.3% credible interval from this posterior density function is $H_0 = 70.0^{+12.0}_{-8.0}$ km s^{-1}Mpc^{-1}. The 68.3% (1σ) and 95.4% (2σ) minimal credible intervals are indicated by dashed and dotted lines, respectively.

Tension between
- CMB measurements from Planck
(67.74 ± 0.46 km/s/Mpc)
- SNIa measurements
from SHoES21
(73.24 ± 1.74 km/s/Mpc)

1. Parameter estimation of the GW source
→ luminosity distance d_L

2. Optical transient identified: source at 10 arcsec from the galaxy NGC 4993
→ peculiar velocity

3. Redshift of the electromagnetic spectrum
→ cosmological expansion rate v_H

4. Hubble-law
(valid up to 50 Mpc): $v_H = H_0\, d_L$
→ Hubble constant

TESTING GENERAL RELATIVITY

What is the problem with GR?

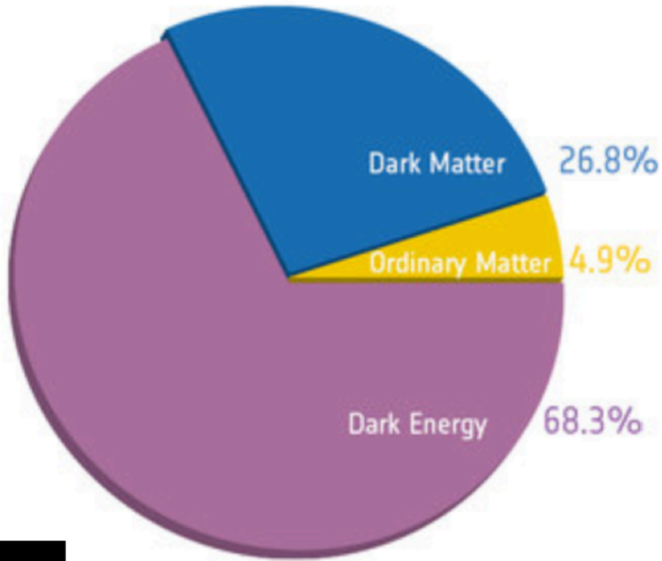

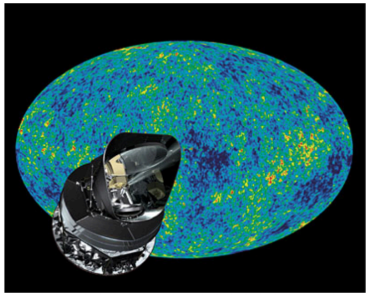

After Planck

→ Both DM and DE interact only gravitationally

→ Hope to test EFT in the near future

→ Need for modifying GR !

<u>No dark matter detected:</u>

2000 - MACHO (microlensing)
2014, 2016 - WIMP particles (LUX, PandaX-II, Xenon100)
2015 - Axions (Axion Dark Matter Experiment, Centre for Experimental Nuclear Physics and Astrophysics (CENPA), University of Washington)
2016 - Sterile neutrinos (IceCube)
2016 - Extra dimensions (LHC)
2016 - Supersymmetric particles (LHC)
2019 - stau, Higgsino not found (ATLAS, LHC)

<u>Dark energy:</u> Cosmological constant?

But this vacuum energy density is 60 orders of magnitude smaller than the theoretical prediction of zero-point energy in quantum field theory

<u>Quantum gravity:</u> several attempts, no established final theory

Its low energy (infrared) limit should give GR and corrections at first order —> effective field theory (EFT)

What else is the problem with GR?

4) Highly non-renormalizable,

can not be formulated as a QFT as for the other fundamental forces,
can not directly be embedded into the standard model of particle physics

5) Early universe inflation requires additional field(s),

best fit with CMB data given by Einstein gravity with an inflaton field (slow-roll model with a concave potential)

Y. Akrami *et al.* [Planck Collaboration], "Planck 2018 results. X. Constraints on inflation," arXiv:1807.06211 [astro-ph.CO].

6) Tensions in the determination of the Hubble-parameter

CMB measurements from Planck:

67.74 ± 0.46 km/s/Mpc

SNIa measurements from SH0ES21:

73.24 ± 1.74 km/s/Mpc

GW170817 luminosity distance and optical transient:

$70.0^{+12.0}_{-8.0}$ km/s/Mpc

nature Accelerated Article Preview

LETTER

doi:10.1038/nature24471

A gravitational-wave standard siren measurement of the Hubble constant

The LIGO Scientific Collaboration and The Virgo Collaboration*, The 1M2H Collaboration*, The Dark Energy Camera GW-EM Collaboration and the DES Collaboration*, The DLT40 Collaboration*, The Las Cumbres Observatory Collaboration*, The VINROUGE Collaboration* & The MASTER Collaboration*

RESEARCH LETTER

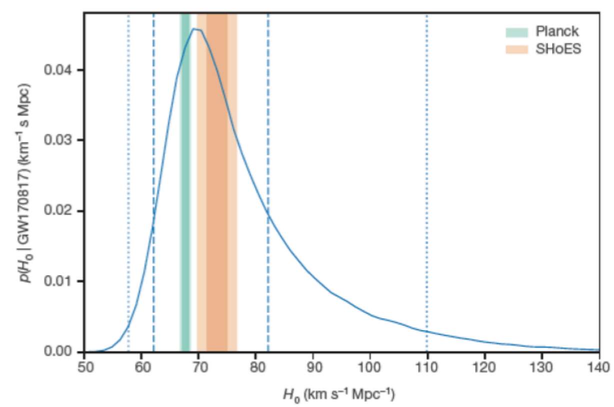

Figure 1 | GW170817 measurement of H_0. The marginalized posterior density for H_0, $p(H_0 \mid GW170817)$, is shown by the blue curve. Constraints at 1σ (darker shading) and 2σ (lighter shading) from Planck[20] and SHoES[21] are shown in green and orange, respectively. The maximum a posteriori value and minimal 68.3% credible interval from this posterior density function is $H_0 = 70.0^{+12.0}_{-8.0}$ km s^{-1} Mpc^{-1}. The 68.3% (1σ) and 95.4% (2σ) minimal credible intervals are indicated by dashed and dotted lines,

7) Problems in defining gravitational energy-momentum, null boundary terms in the action, occurrence of singularities...

How to go beyond GR?

- By relaxing one of the fundamental hypotheses of the Lovelock theorem that makes Einstein theory unique:

- invariance under diffeomorphisms,

  (ex: Lorentz-invariance breaking, massive gravity)

- locality,

- pure metric formulation in four space-time dimensions

  (add new fields, representing gravity, ex: scalar-tensor theories)

- In general they contain one or more extra d.o.f-s, used to

- describe dark energy (fifth force)

- make the theory renormalizable (cure the UV problem of GR)

- Requirements:

- compatibility with observations (Solar System, etc...)

- stability → perturbations

GW Test 1: Massive graviton modifies dispersion relations

Selected for a Viewpoint in *Physics*
PRL **116,** 221101 (2016) PHYSICAL REVIEW LETTERS

Tests of General Relativity with GW150914

B. P. Abbott *et al.**
(LIGO Scientific and Virgo Collaborations)
(Received 26 March 2016; revised manuscript received 9 May 2016; published 31 May 2016)

For massive graviton dispersion relations: $E^2 = p^2c^2 + m_g^2c^4$

Compton-wavelength: $\lambda_g = h/(m_g c)$

Speed (energy) dependent frequency (wavelength):

$$v_g^2/c^2 \equiv c^2p^2/E^2 \simeq 1 - h^2c^2/(\lambda_g^2 E^2)$$

Newtonian potential with Yukawa-corrections

$$\varphi(r) = \frac{GM}{r}\left[1 - e^{-\frac{r}{\lambda_g}}\right]$$

Modified GW phase:

$$\Phi_{MG}(f) = -(\pi D c)/[\lambda_g^2(1+z)f]$$

(in LCDM, influence on binary dynamics neglected)

C. M. Will, Phys. Rev. D 57, 2061 (1998).

—> From the arrival time-difference between the two LIGO detectors the Compton-wavelength of graviton is constrained from below: 10^{13} km !

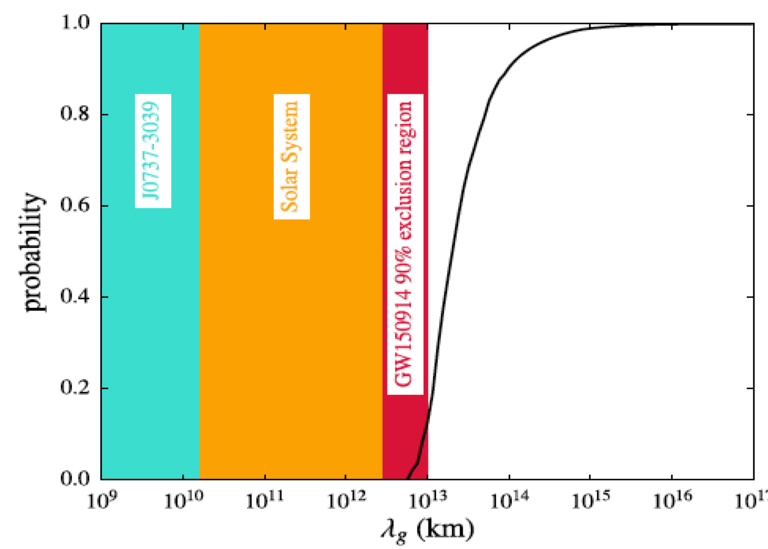

$$\boxed{m_g \leq 1.2 \times 10^{-22}\ \mathrm{eV}/c^2.}$$

GW Test 2: Local Lorentz-invariance confirmed

Modified dispersion relation:

$$E^2 = p^2c^2 + Ap^\alpha c^\alpha,\ \alpha \geq 0,$$

S. Mirshekari, N. Yunes, and C. M. Will, Phys. Rev. D 85, 024041 (2012).

Massive graviton theories: $(\alpha = 0,\ A > 0)$
Multifractal space-times: $(\alpha = 2.5)$
Doubly special relativity: $(\alpha = 3)$,
Hořava-Lifsic and extra dimensions: $(\alpha = 4)$

Speed (energy) dependent frequency (wavelength):

$$v_g/c = 1 + (\alpha - 1)AE^{\alpha-2}/2$$

N. Yunes, K. Yagi, and F. Pretorius, Phys. Rev. D 94, 084002 (2016).

Lorentz-invariance violation and massive graviton could be tested in the same time !

Compare to experim. limits on gluon mass < 2x10^{-4} eV/c^2 !!

PRL 118, 221101 (2017) PHYSICAL REVIEW LETTERS

GW170104: Observation of a 50-Solar-Mass Binary Black Hole Coalescence at Redshift 0.2

B. P. Abbott et al.*
(LIGO Scientific and Virgo Collaboration)
(Received 9 May 2017; published 1 June 2017)

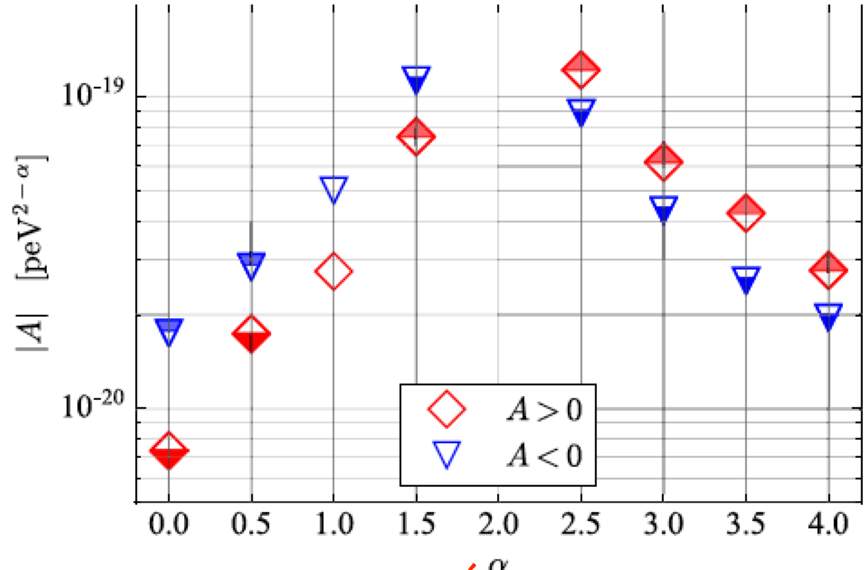

Strong constraint on Lorentz-invariance violation from GW-s !

From first 3 detected GW-s:

$$\lambda_g > 1.6 \times 10^{13}\ \text{km},$$
$$m_g \leq 7.7 \times 10^{-23}\ \text{eV}/c^2.$$

GW Test 3: PN coefficients checked

Selected for a Viewpoint in *Physics*

PRL **116,** 221101 (2016) PHYSICAL REVIEW LETTERS

Tests of General Relativity with GW150914

B. P. Abbott *et al.*[*]

(LIGO Scientific and Virgo Collaborations)

(Received 26 March 2016; revised manuscript received 9 May 2016; published 31 May 2016)

Inspiral-merger-ringdown test:

Modified waveforms in parametric form

GW did not deviate significantly from GR prediction !

Confirmed the values of the PN coefficients !

Note: Brans-Dicke theory would generate a new kind of PN coefficient, still GWs gave much milder constraint on the BD parameter, than Solar System tests

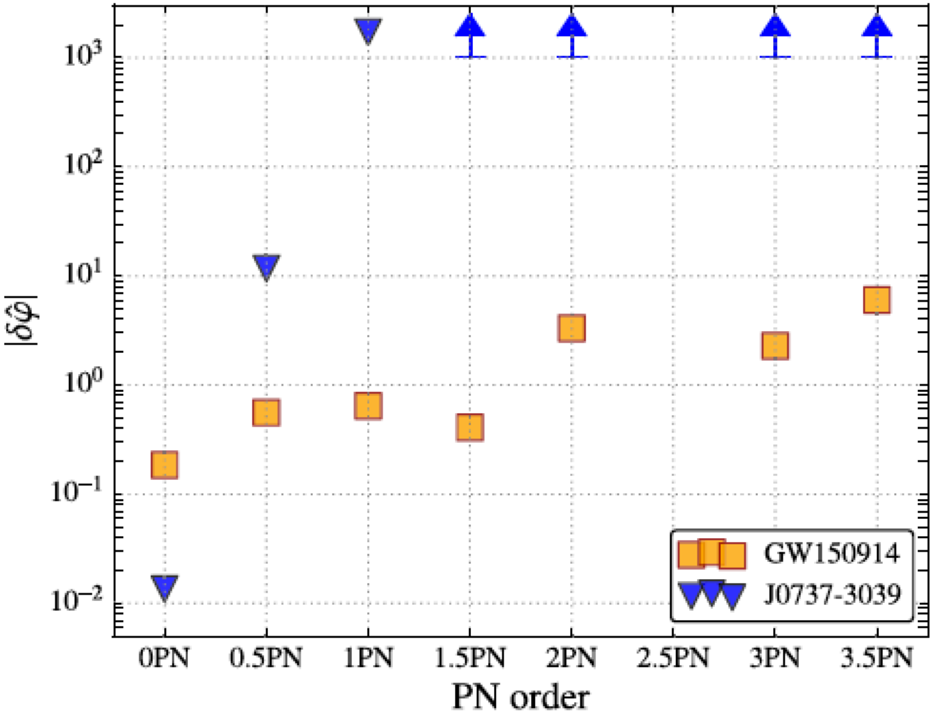

GW Test 4: polarisation check

waveform = Σ_i antenna function$_i$ x polarisation mode$_i$

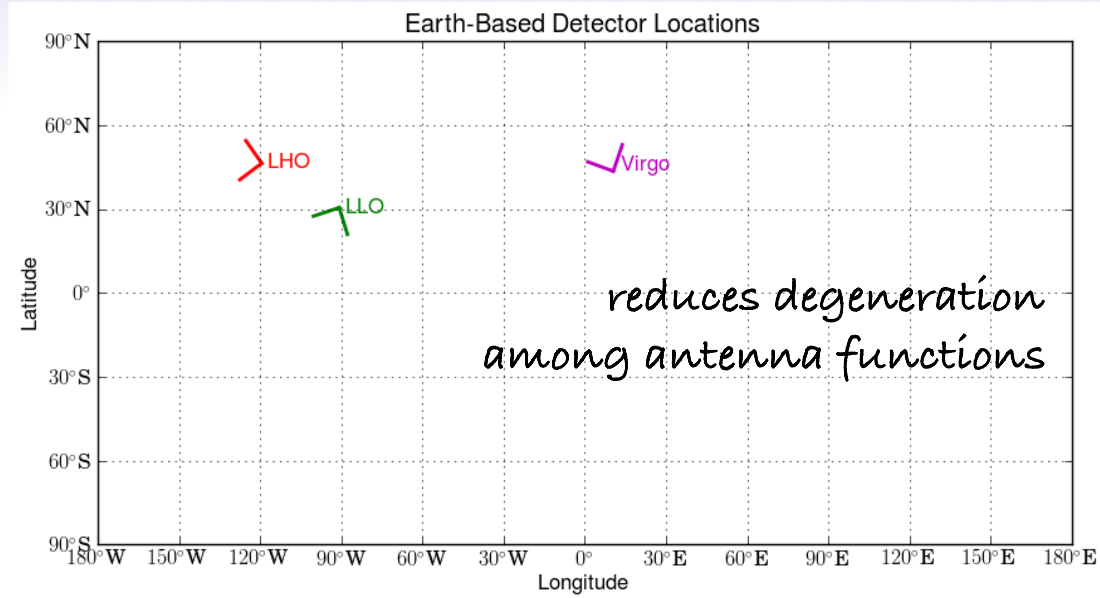

reduces degeneration among antenna functions

Preliminary result (toy-model):

GW purely vector
(Bayes-factor 200 times smaller)
GW purely scalar
(Bayes-factor 1000 times smaller than the one given by GR)
GW purely tensorial

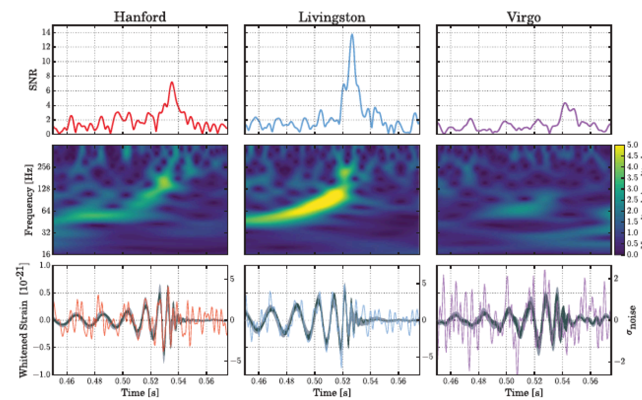

More serious analysis needed, combining such DoF and looking for the probability of their coexistence in various compositions

Phys. Rev. Lett. **119**, 141101 (2017)

Constraints on Horndeski theory from GW170817

GW propagation speed agrees with the speed of light at the order of one part in quadrillionth at low redshifts

1. Theories with dependence of the kinetic term X in the coupling of the Ricci curvature R and Einstein tensor G_{mn} in L_4 and L_5 are disruled
2. L_5 does not depend on ϕ either (except through its derivatives)
3. due to the Bianchi identities, the whole L_5 vanishes

$$L^{\mathrm{H}} = \sum_{i=2}^{5} L_i^{\mathrm{H}}, \tag{4.4}$$

where

$$L_2^{\mathrm{H}} = G_2(\phi, X), \tag{4.5}$$

$$L_3^{\mathrm{H}} = G_3(\phi, X)\Box\phi, \tag{4.6}$$

$$L_4^{\mathrm{H}} = G_4(\phi, \cancel{X})R \cancel{- 2G_{4X}(\phi, X) \times [(\Box\phi)^2 - \nabla^a\nabla^b\phi\nabla_a\nabla_b\phi]}, \tag{4.7}$$

$$L_5^{\mathrm{H}} = \cancel{G_5(\phi, X)G_{ab}\nabla^a\nabla^b\phi + \frac{1}{3}G_{5X}(\phi, X)[(\Box\phi)^3 - 3(\Box\phi)\nabla^a\nabla^b\phi\nabla_a\nabla_b\phi + 2\nabla_a\nabla_b\phi\nabla^c\nabla^b\phi\nabla_c\nabla^a\phi]}. \tag{4.8}$$

LIGO, Virgo, and partners make first detection of gravitational waves and light from colliding neutron stars

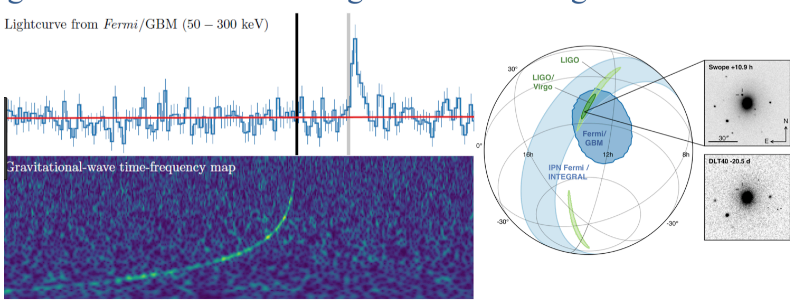

Kobayashi, T.; Yamaguchi, M.; Yokoyama, J., Prog. Theor. Phys. 2011, 126, 511–529.
De Felice, A.; Tsujikawa, S., JCAP 2012, 007.
Baker, T.; Bellini, E.; Ferreira, P.G.; Lagos, M.; Noller, J.; Sawicki, I., Phys. Rev. Lett. 2017, 119, 251301.
Ezquiaga, J.M.; Zumalacarregu, M., Phys. Rev. Lett. 2017, 119, 251304.
Creminelli, P.; Vernizzi, F. Phys. Rev. Lett. 2017, 119, 251302.

Constraints and their prospects

5 parameters for deviations from LCDM of the beyond Horndeski theories:

$$\{\alpha_M, \alpha_K, \alpha_B, \alpha_H, \alpha_T\}$$

Last one is approximately zero due to GW observations

Third and fourth constrained by astrophysical measurements

First gives the running of the Planck mass

– constrain it from time variations of the Newton constant

Second the kinetic term for the scalar

- constrain it from Strong Equivalence Principle violation

They are the parameters of the EFT of dark energy

Constraining them better is one of the goals of the future missions

DESI, LSST, Euclid and WFIRST

DESI, 2019 — Dark Energy Spectroscopic Instrument (Arizona)

LSST, 2019 — Large Synoptic Survey Telescope (Chile)

Euclid, 2021 — Euclid Mission (ESA & Euclid Consortium)

WFIRST, 2025? — Wide Field Infrared Survey Telescope (NASA)

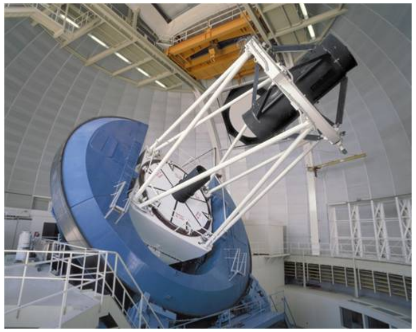

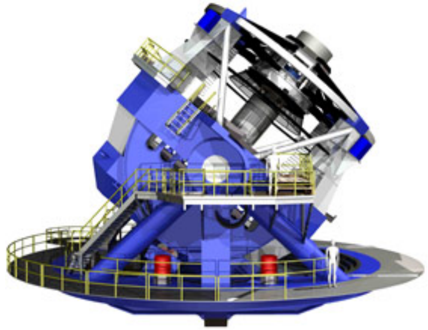

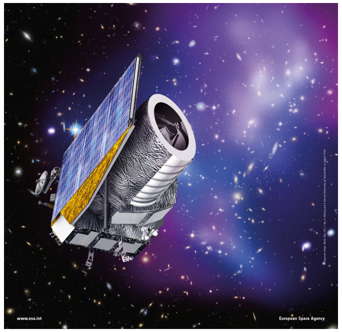

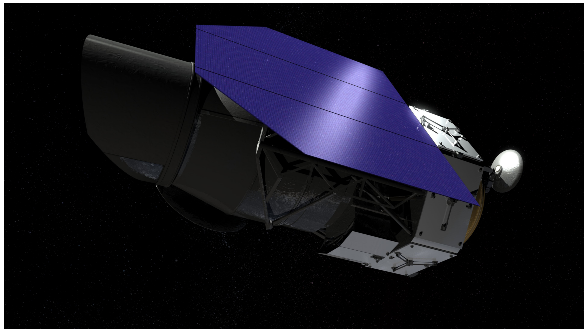

MULTIMESSENGER APPROACH
(INCLUDING RADIO)

Multimessenger approach to SMBH binary coalescence

Likely scenario:

1. Inspiraling SMBH binary, with typical mass ratio 1:3 to 1:30

2. The Spin-flip occurs due to gravitational radiation reaction

3. The GW signal amplitude and frequency gradually increases (detectable by LISA, at least in the lower SMBH mass range)

4. The SMBH-s merge, the newly formed SMBH will have a different spin direction, along which a new, energetic jet will be gradually formed, with increasing activity in all frequencies

5. The UHECR, HE neutrino emission

6. Luminous radio afterglow with flat spectrum extending to near THz frequencies

1. Analysis of 18 ys of VLBI data of the quasar S5 1928+738 (pre-merger binary)

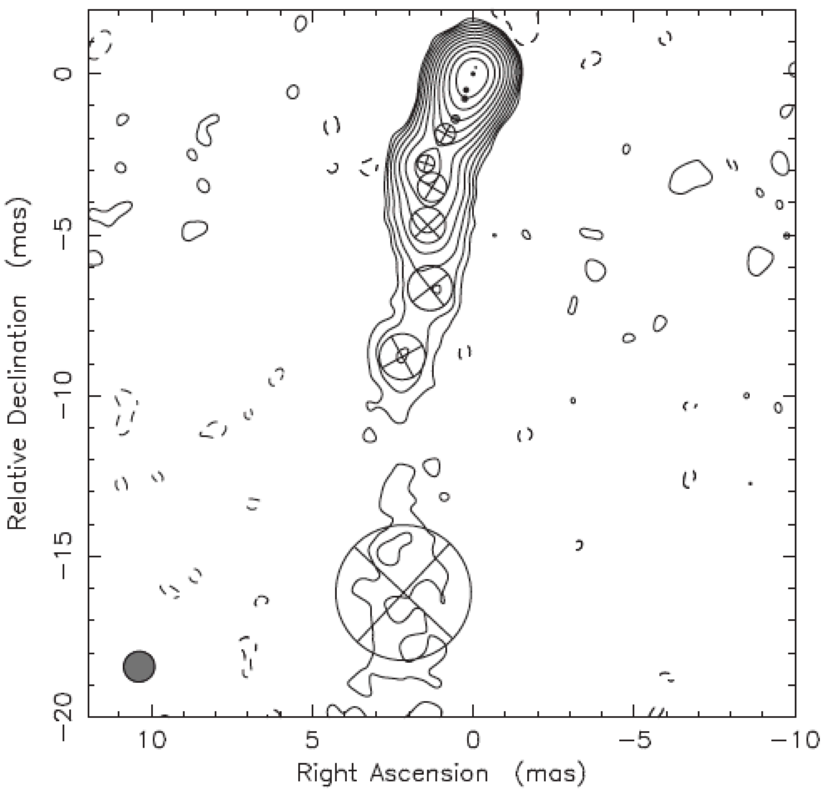

Figure 1. Model-fits to the 2013.06 epoch of MOJAVE observation of S5 1928+738 at 15 GHz. The core lies at 0, 0 coordinates. Contours are in per cent of the peak flux 2.18 Jy beam^{-1} and they increase by factors of 2. The lowest contour level is 1.1 mJy beam^{-1} (0.05 per cent of the peak flux). The off-source rms noise is 0.16 mJy beam^{-1}. The restoring beam size is shown in the bottom-left corner of the image (0.9 mas × 0.9 mas). Each circle on the map corresponds to a model-fit component. Their sizes represent the FWHM of the fitted Gaussian. Tapered image was created in DIFMAP.

Geometric model of a helical structure projected onto the plane of the sky

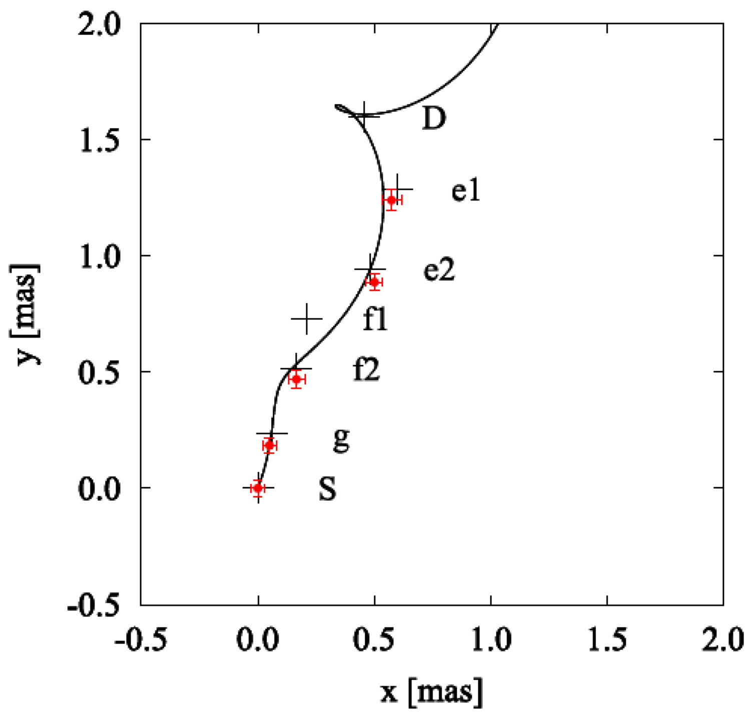

Figure 4. Black crosses denote the 43 GHz model components derived by Lister & Smith (2000, their sizes are not representative of the errors), red dots with error bars denote the 15 GHz model components. In the figure, north is oriented towards negative y values. We complement the data by five of the seven component positions identified at 15 GHz. The black curve represents the 'starting jet model' (see Section 4.2) fitted to the 43 GHz data.

A spinning supermassive black hole binary model consistent with VLBI observations of the S5 1928+738 jet
E. Kun, K. É . Gabányi, M. Karouzos, S. Britzen, L. Á. Gergely, MNRAS **445,** 1370–1382 (2014)

1. Periodic + linear variabilities

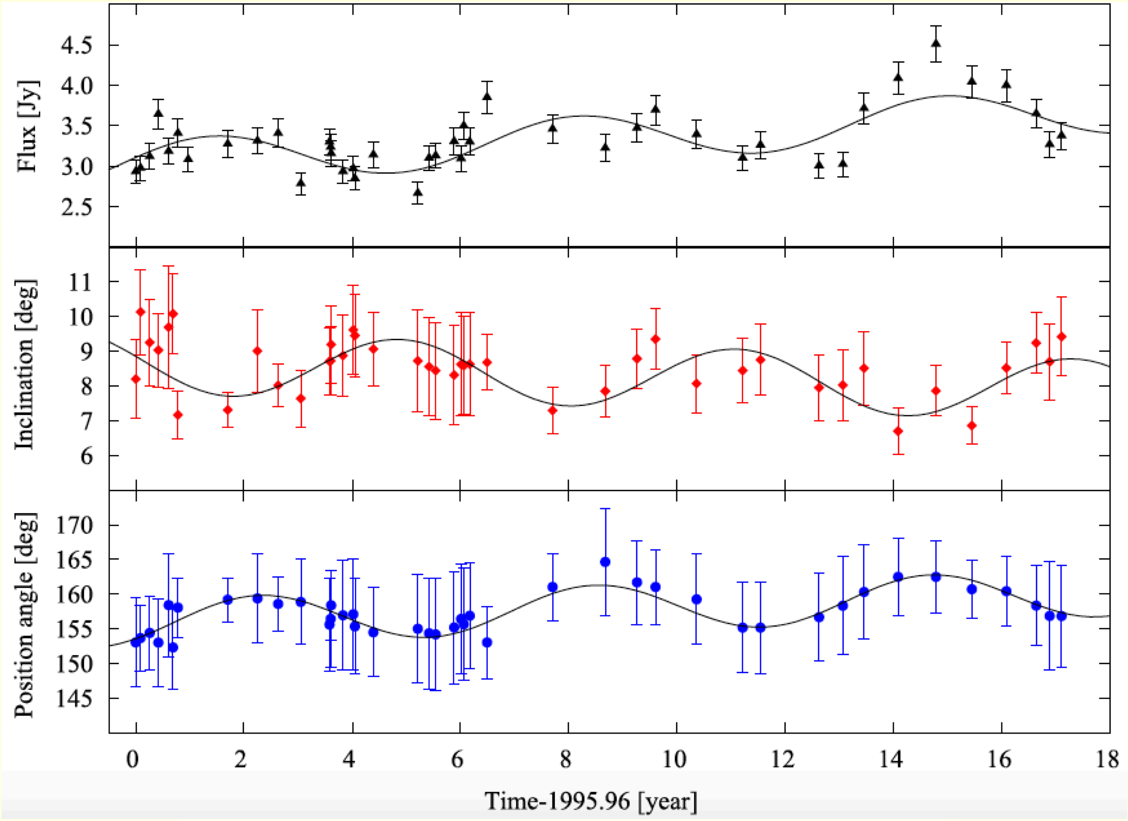

- Variation of the inclination of the inner 2 mas of the jet = a periodic term with amplitude of ~0.°89 + a linear decreasing trend with rate of ~0.°05 yr^{-1}
- Variation of the position angle = a periodic term with amplitude of ~3.°39 + a linear increasing trend with rate of ~0.°24 yr^{-1}

A spinning supermassive black hole binary model consistent with VLBI observations of the S5 1928+738 jet
E. Kun, K. É . Gabányi, M. Karouzos, S. Britzen, L. Á. Gergely, MNRAS **445,** 1370–1382 (2014)

1. Orbital, mass and spin parameters

- The periodic components generated by the orbital motion of a BBH inspiraling at the jet base
- Linear trends arise from the slow reorientation of the spin of the jet emitter black hole induced by the spin–orbit (SO) precession
- First detection of the spin of a jet-emitting BH in a binary from VLBI jet kinematics

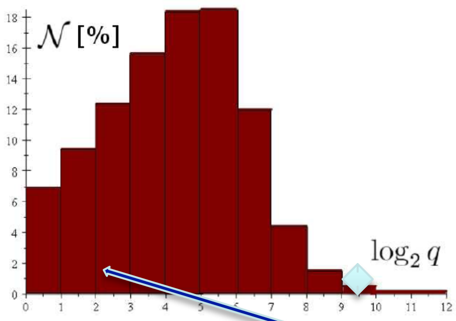

FIG. 2: (Color online) The number of SMBH encounters with mass ratios q as function of $\log_2 q$.

Mass ratio in the typical range !

Table 6. Binary parameters.

Total mass, m^a ($M_\odot$)	8.13×10^8
Orbital period, T (yr)	4.78 ± 0.14
Binary separation, r (pc)	0.0128 ± 0.0003
PN parameter, ε	≈ 0.003
Mass ratio, ν	$[0.21 : 1/3]$
Spin–orbit precession period, T_{SO} (yr)	4852 ± 646
Gravitational lifetime, T_{merger} (yr)	$(1.44 \pm 0.19) \times 10^6$

[a] independent result by Woo & Urry (2002).

A spinning supermassive black hole binary model consistent with VLBI observations of the S5 1928+738 jet
E. Kun, K. É . Gabányi, M. Karouzos, S. Britzen, L. Á. Gergely, MNRAS **445,** 1370–1382 (2014)

2. The spin-flip in typical mass-ratio binaries

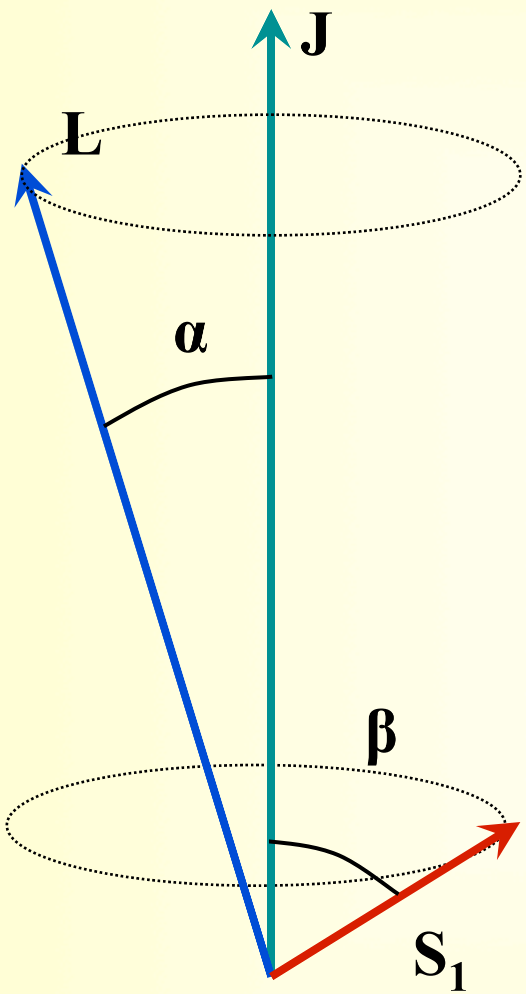

- *due to GW emission* the spin aligns to the original **J** direction

The spin-flip phenomenon in supermassive binary black hole mergers
L. Á. Gergely, P. L. Biermann,
Astrophys. J. **697,** 1621 (2009)

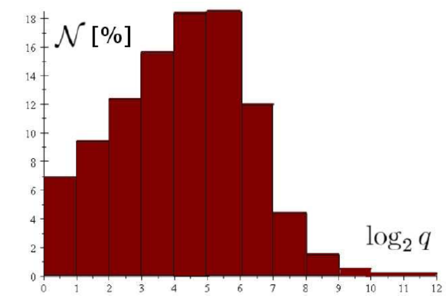

FIG. 2: (Color online) The number of SMBH encounters with mass ratios q as function of $\log_2 q$.

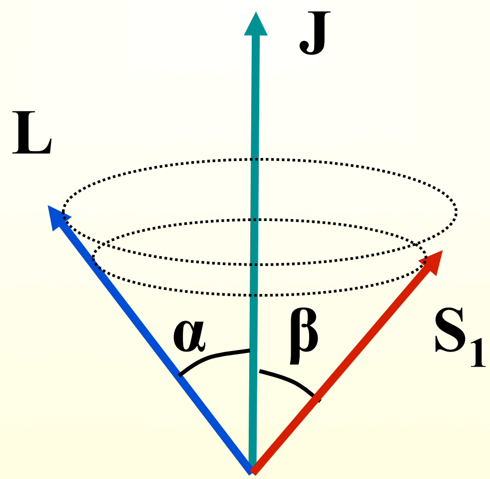

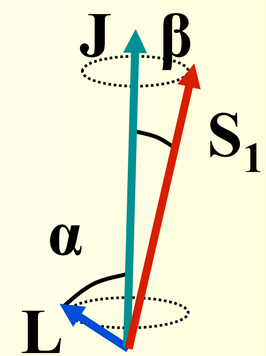

Key elements: (i) typically the BHs are not equal mass, $m_2 << m_1$, neglect $S_2 \sim m_2^2$

(ii) the direction of **J** is conserved, (iii) the magnitude of $\mathbf{S_1}$ is conserved → spin-flip

3. LISA (Laser Interferometer Space Antenna) – 2034 ESA

3 satellites on Earth-following orbit, arm length 2.5 million km
able to detect 0.1 mHz to 100 mHz GWs
from binary SMBHs (lower mass end), relics from Big Bang, ⋯

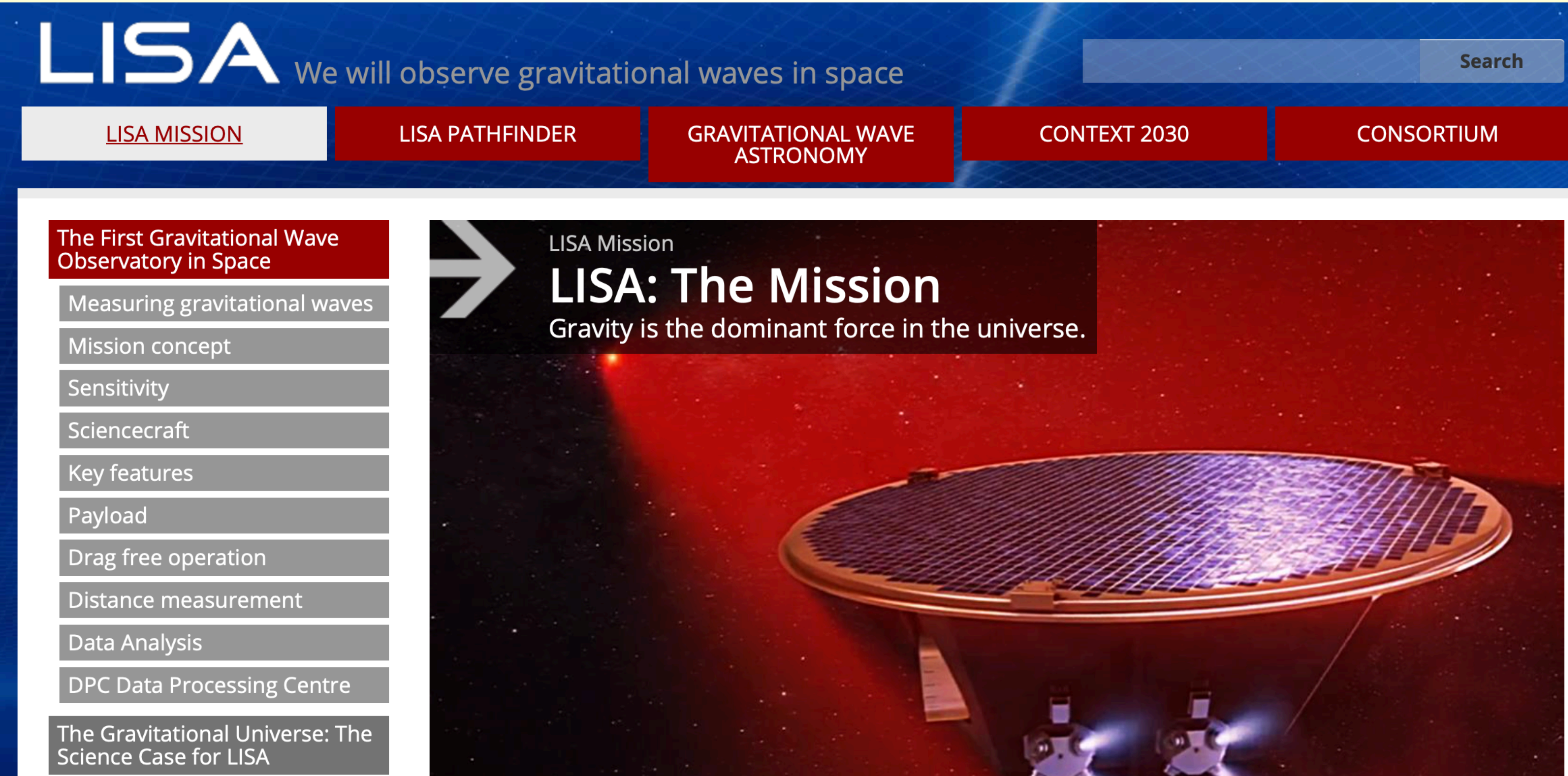

3. LISA Pathfinder: successful testing of the LISA technology

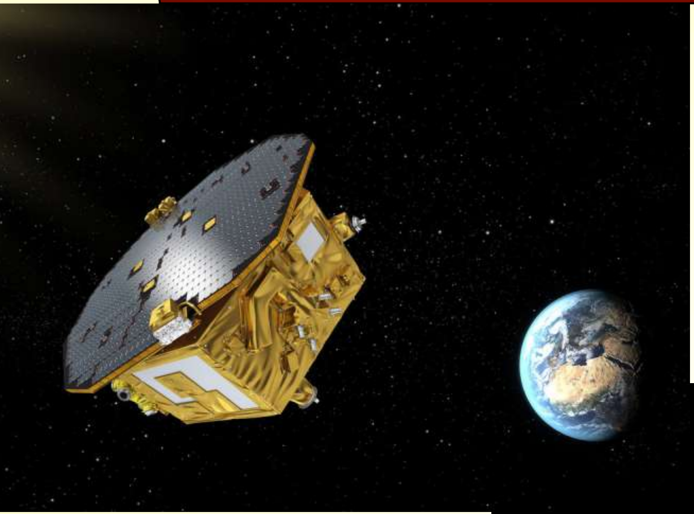

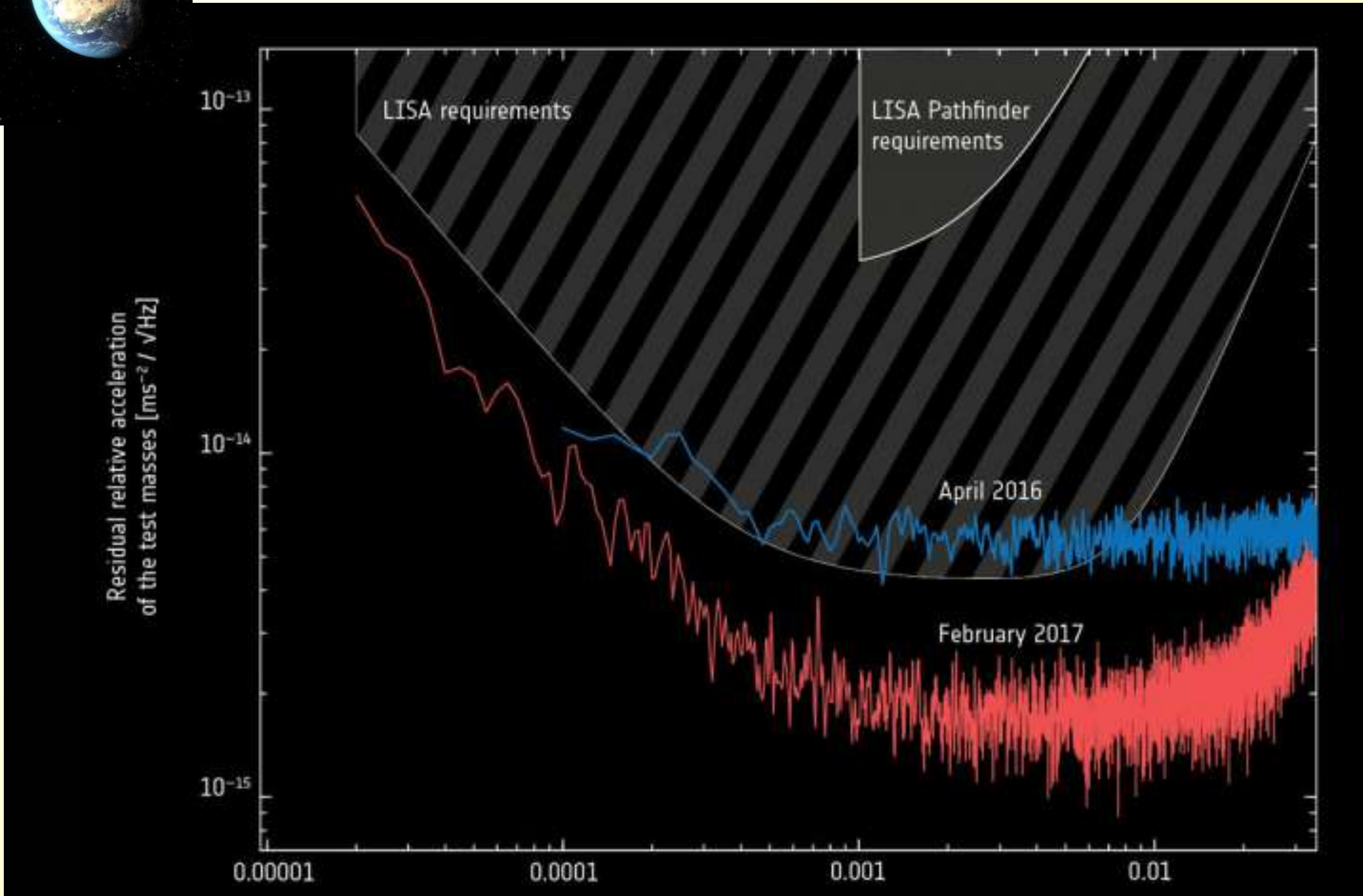

4. X-shaped radio galaxies: surviving witnesses of coalescing SMBH binaries

Old jet-pair:
- steep spectra
- old and slow charged particles

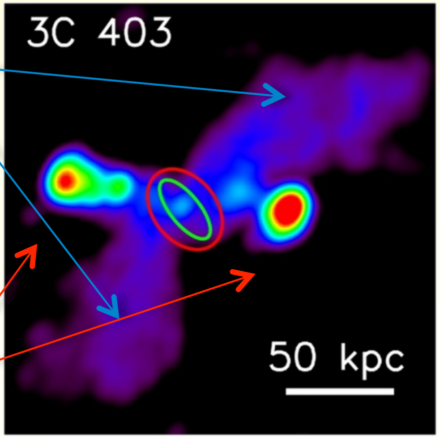

Hodges-Kluck and Reynolds, 2011

New jet-pair:
- bright and flat spectrum
- young and fast charged particles

On the origin of X-shaped radio galaxies
Gopal-Krishna, P. L. Biermann, L. Á. Gergely, P. J. Wiita,
Research in Astron. Astrophys. **12**, 127–146 (**2012**)

Spin-flip model:	wing formation ceases before the primary lobes begin to form
Description	Jet direction flips due to re-alignment of the spin of the dominant SMBH, due to its merger with another SMBH.
Key merit/evidence	⁎ Explains why hotspots are never seen in both lobe pairs. ⁎ Can explain secondary lobes being larger than primary lobes. ⁎ Post spin-flip, jets can easily propagate straight outwards. ⁎ Z-symmetry of the wings can be easily understood. ⁎ The empirically inferred systematic excess of SMBH mass in XRGs (compared to those in RGs) fits naturally into this picture. ⁎ Can also explain the formation of superdisks.
Does not naturally explain	⁎ The correlation of the radio lobe axis with the optical axis of the host elliptical.

4. XRG catalog, many as post spin-flip radio galaxies

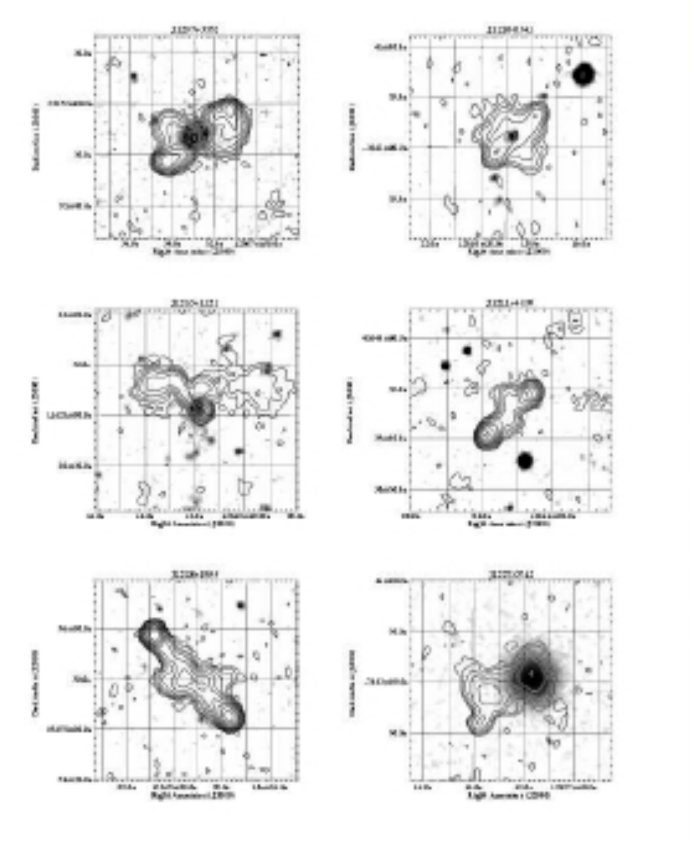

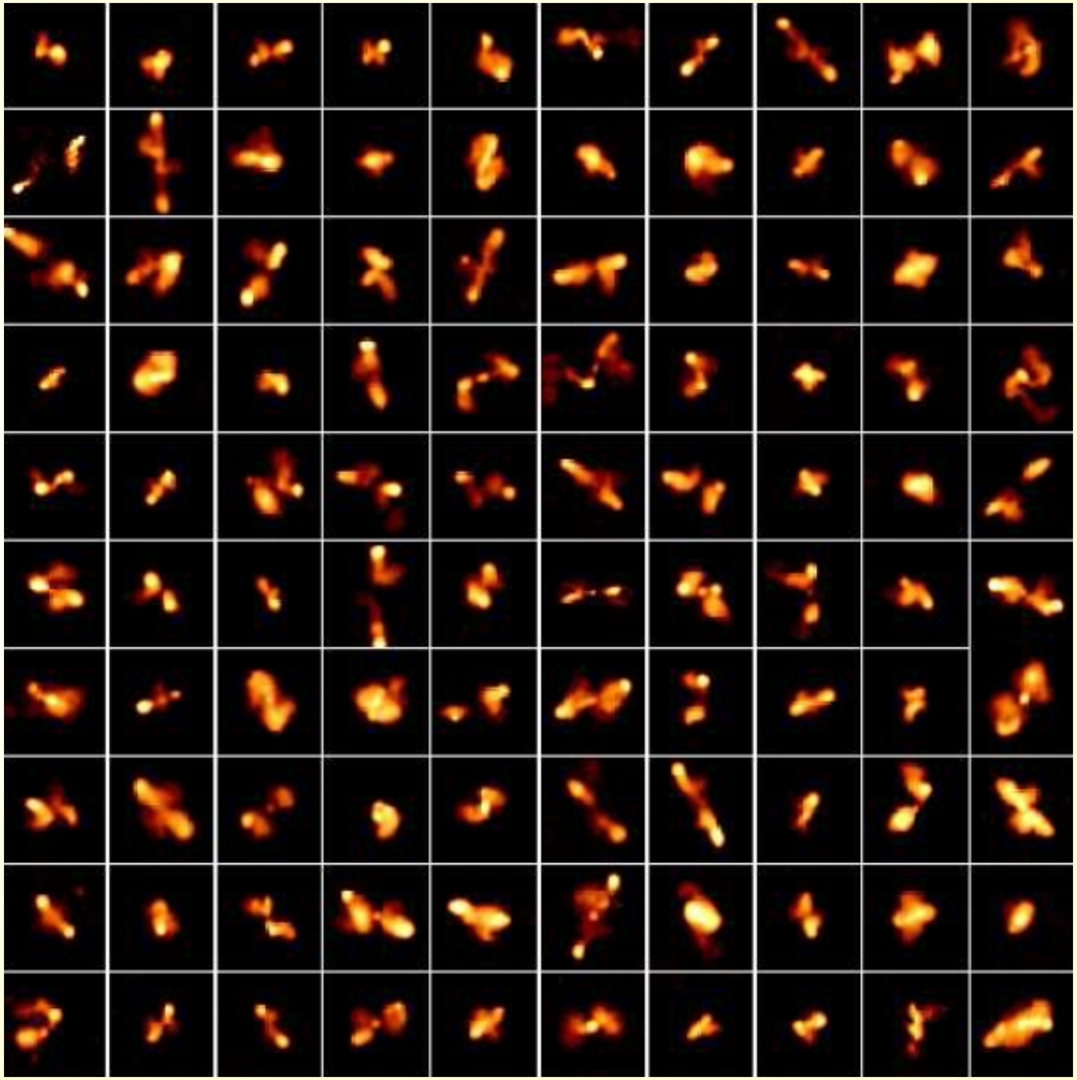

Cheung, C. C. :The Astronomical Journal, 133, 2097-2121 (2007), arXiv:astro-ph/0701278v3

5. Track-type and shower-type HE neutrino events (IceCube)

muon neutrinos → muons

electron neutrinos → electrons

directional uncertainty ~1,2°

Blazar PKS 0723–008
Kun et al., MNRAS Lett. 466, 34, 2017

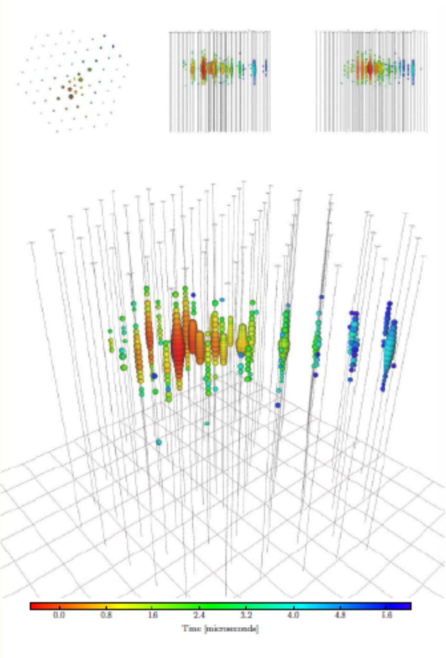

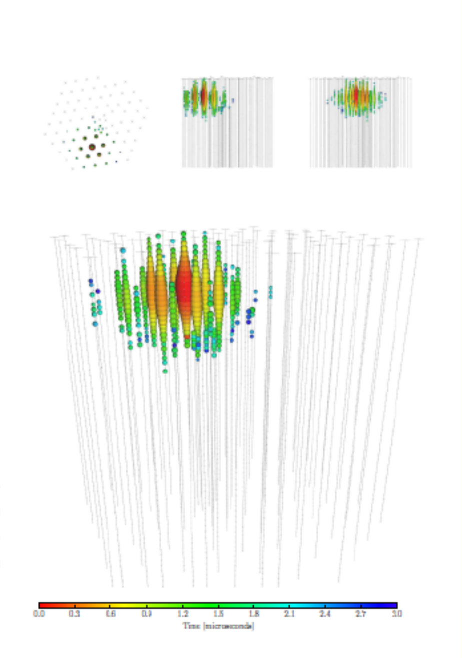

directional uncertainty ~16°

Blazar PKS B1424-418
Kadler et al.,
Nature, 12, 807, 2016

Track-type (e.g. ID5)

Shower-type (e.g. ID35)

6. Radio afterglow and HE neutrinos: the blazar PKS 0723−008

A flat-spectrum candidate for a track-type high-energy neutrino emission event, the case of blazar PKS 0723−008
E. Kun, P. L. Biermann, L. Á. Gergely, MNRAS **466,** L34–L38 (2017)

- AGN positions in radio catalogues (Parkes Catalogue and the Second Planck Catalogue of Compact Sources) cross-correlated with arrival direction (mispointing ~1,2°) of 15 track-type IceCube HE neutrinos
- The blazar PKS 0723–008 was identified as the candidate source of the neutrino event ID5
- Its spectrum is flat up to 857 GHz
- MOJAVE data (15 years)
  - mapping with point sources
  - modeling with Gauss components
  - no component motion detected

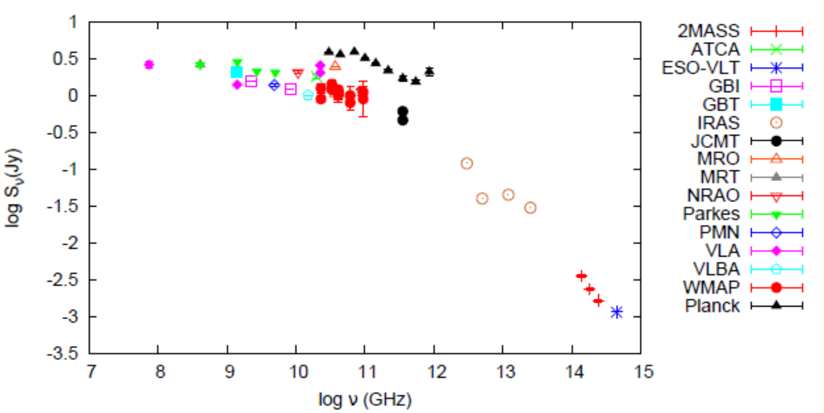

Spectrum of PKS 0723–008 (NASA/IPAC Extragalactic Database)

PCCS2: $\alpha_{30GHz,857GHz}$ = -0,18± 0,04, $\alpha_{70GHz,545GHz}$ = -0,45±0,03

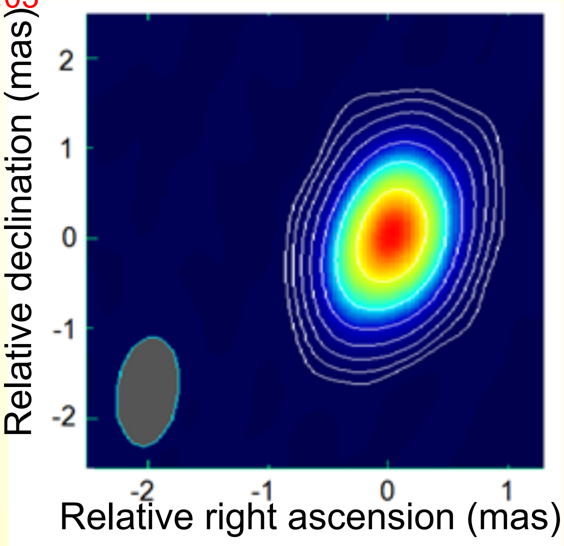

6. Radio afterglow and HE neutrinos: the blazar PKS 0723−008

The neutrino emission is due to energetic proton–proton collisions, where the kinetic energy of the protons is above the energy threshold of pion-creation.

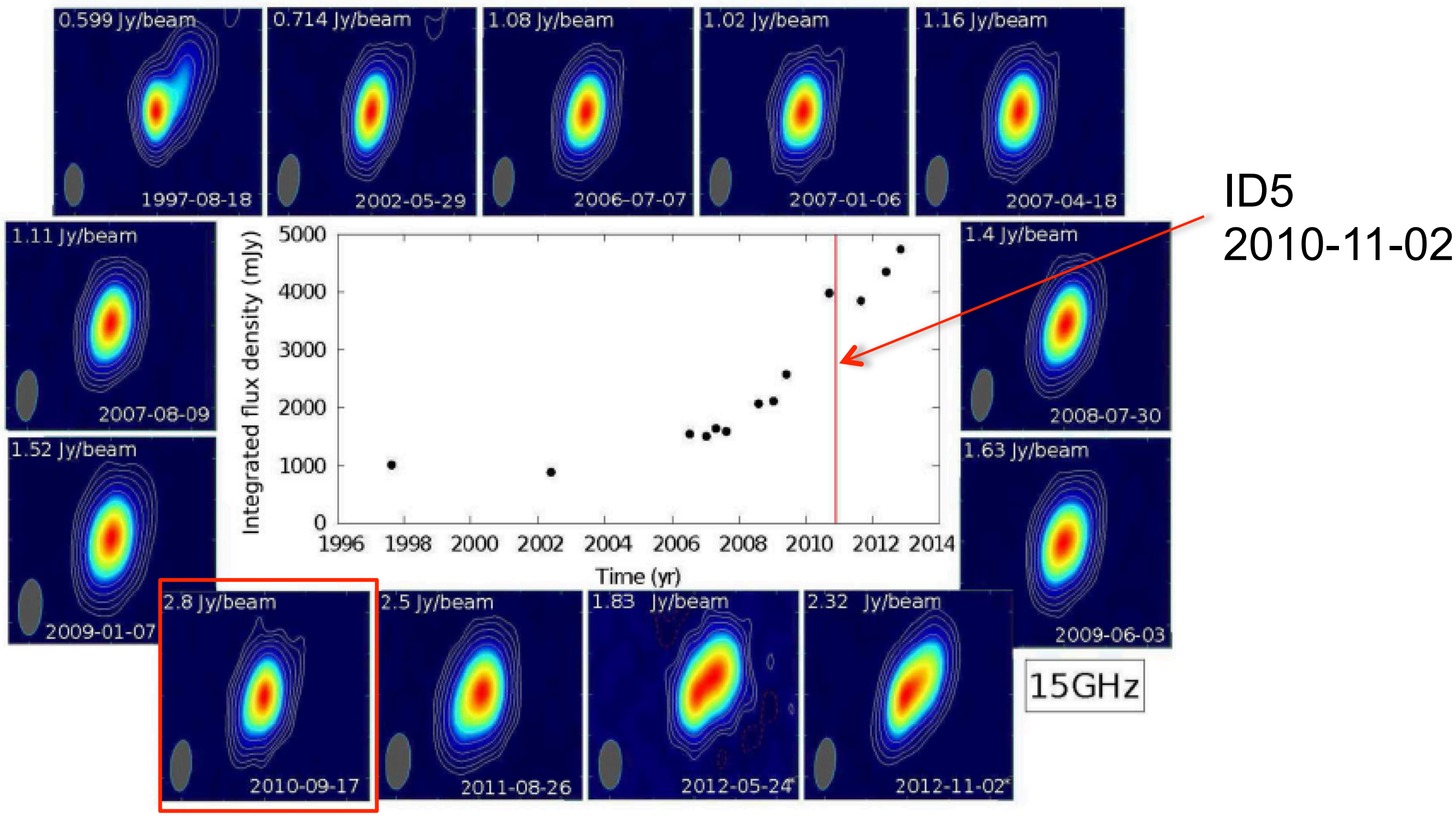

Figure 2. The radio maps of PKS 0723−008 over 12 epochs, represented on logarithmic scale with base 10. They were produced by processing the available VLBA visibilities provided by the MOJAVE team. Iso-flux density contours are in per cent of the peak flux density marked in the left upper corner of the maps. They increase by factors of 1, except the last two epochs (marked by stars), where the contours increase by factors of 2. In the middle, the integrated flux density of the source at 15 GHz is represented as a function of the time. The time of the corresponding neutrino detection (ID5) is indicated by a red vertical line.

A flat-spectrum candidate for a track-type high-energy neutrino emission event, the case of blazar PKS 0723−008
E. Kun, P. L. Biermann, L. Á. Gergely, MNRAS **466,** L34–L38 (2017)

6. TXS 0506+056: γ-rays and the HE neutrino IceCube-170922A

The IceCube Collaboration, Fermi-LAT, MAGIC, AGILE, ASAS-SN, HAWC, H.E.S.S, INTEGRAL, Kanata, Kiso, Kapteyn, Liverpool Telescope, Subaru, Swift/NuSTAR, VERITAS, and VLA/17B-403 teams, Science **361**, 6398 (2018)

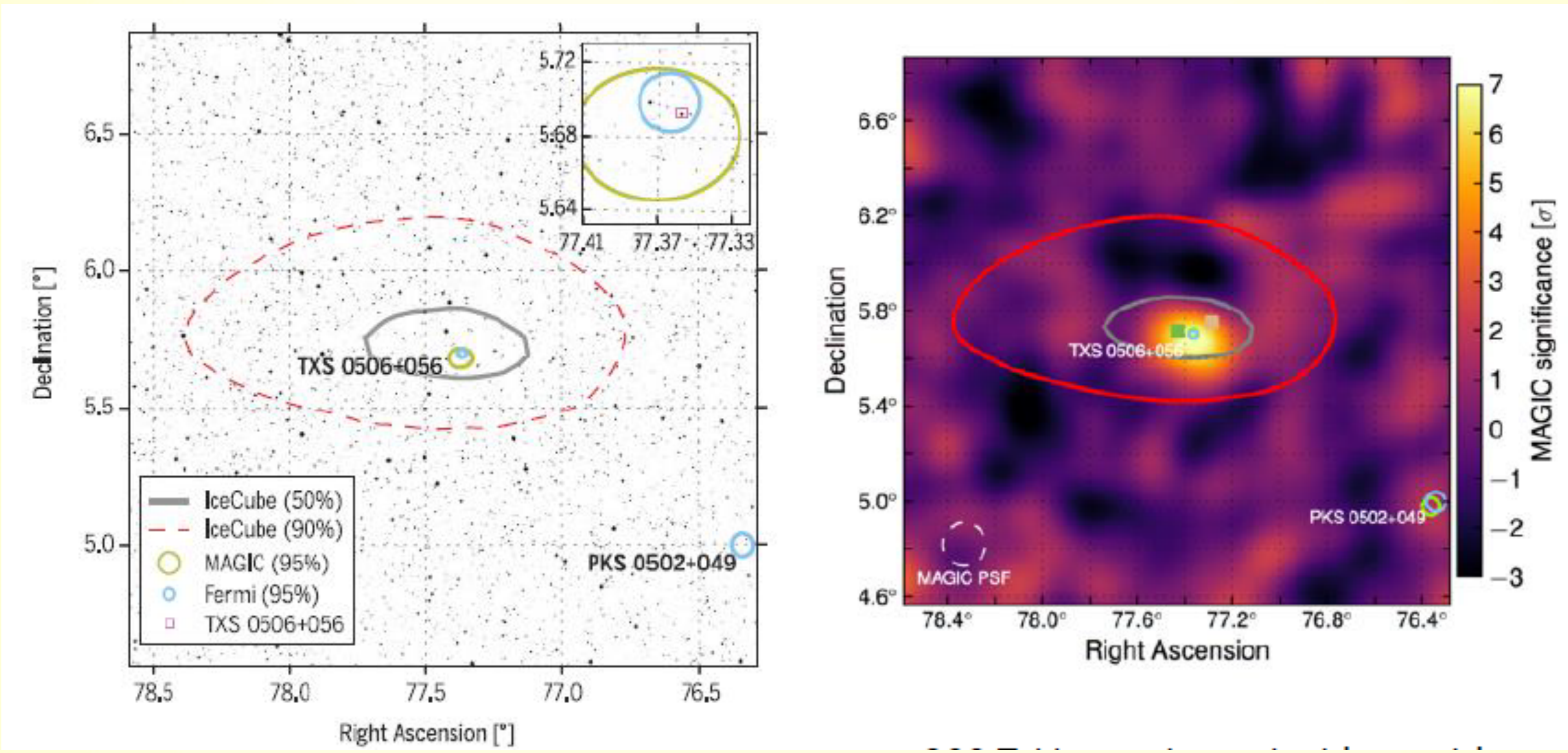

Message: ~300 TeV neutrino (track-type) in spatial and temporal coincidence with a γ-ray flare up to 400 GeV

6. Radio brightening of TXS 0506+056 when HE neutrino IceCube-170922A detected

E Kun, P L Biermann, L Á Gergely, MNRAS Letters **483**, 42 (2018)

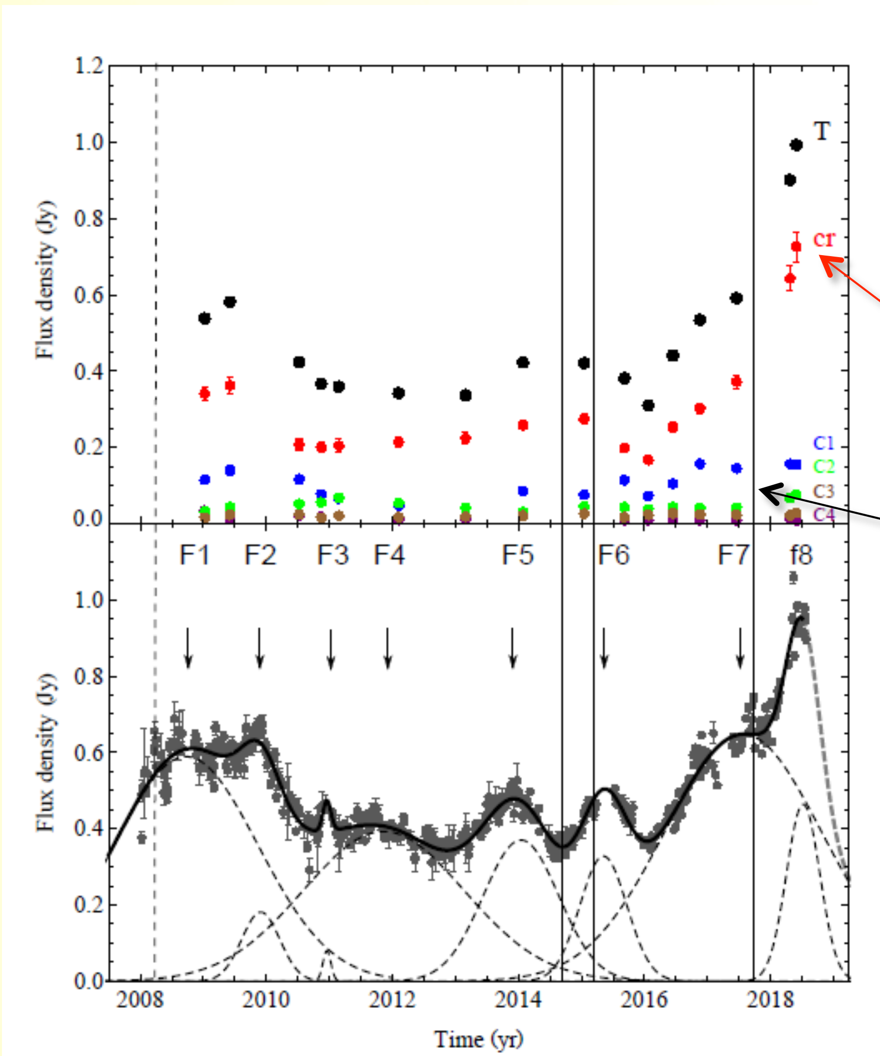

Flux density curve of the jet components (VLBA at 15 GHz)

VLBI core

IceCube-170922A

Gaussian decomposition of OVRO single-dish flux density curves at 15 GHz

Message: the newly formed, energetic jet can be detected both in radio, gamma and as HE neutrinos

Detection of Gravitational Waves: The Future

The near future of GW detection

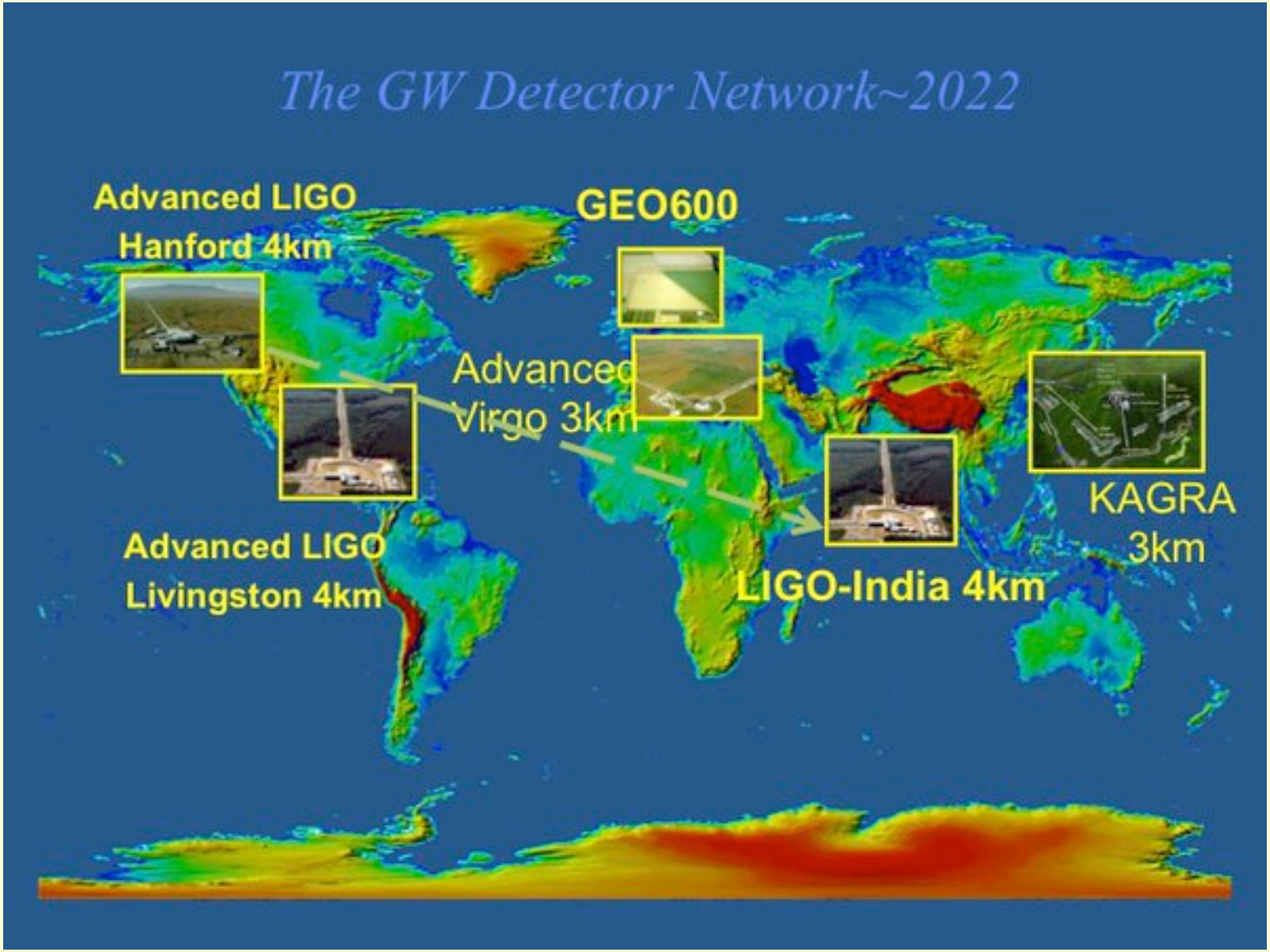

Advanced LIGO + (2024+)

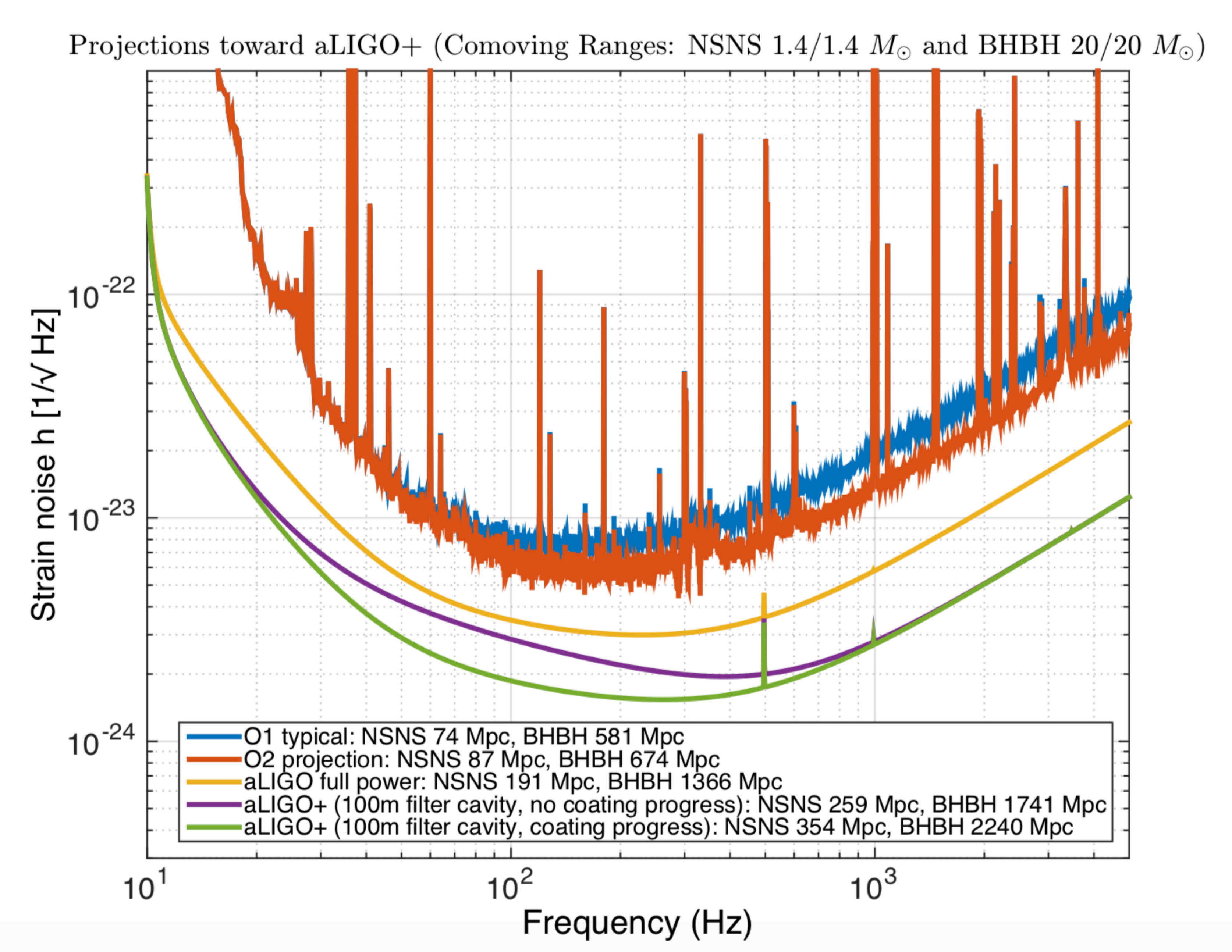

Einstein telescope (planned, somewhere in Europe)

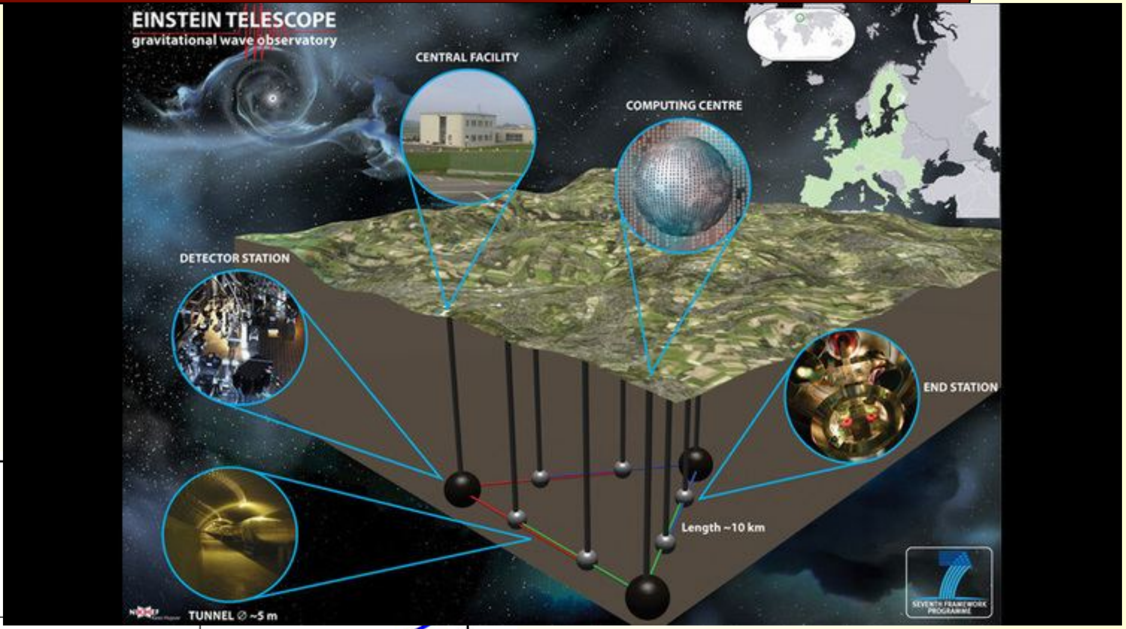

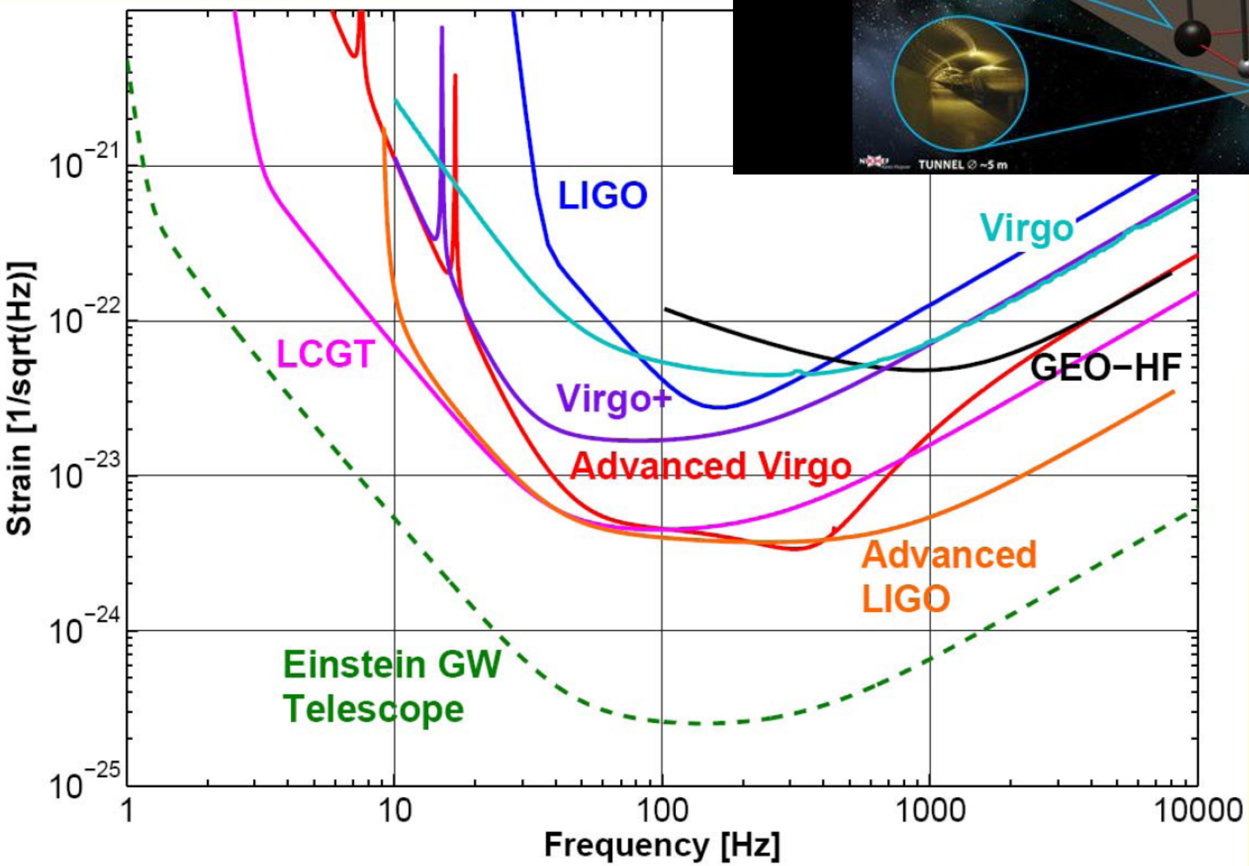

The gravitational wave spectrum

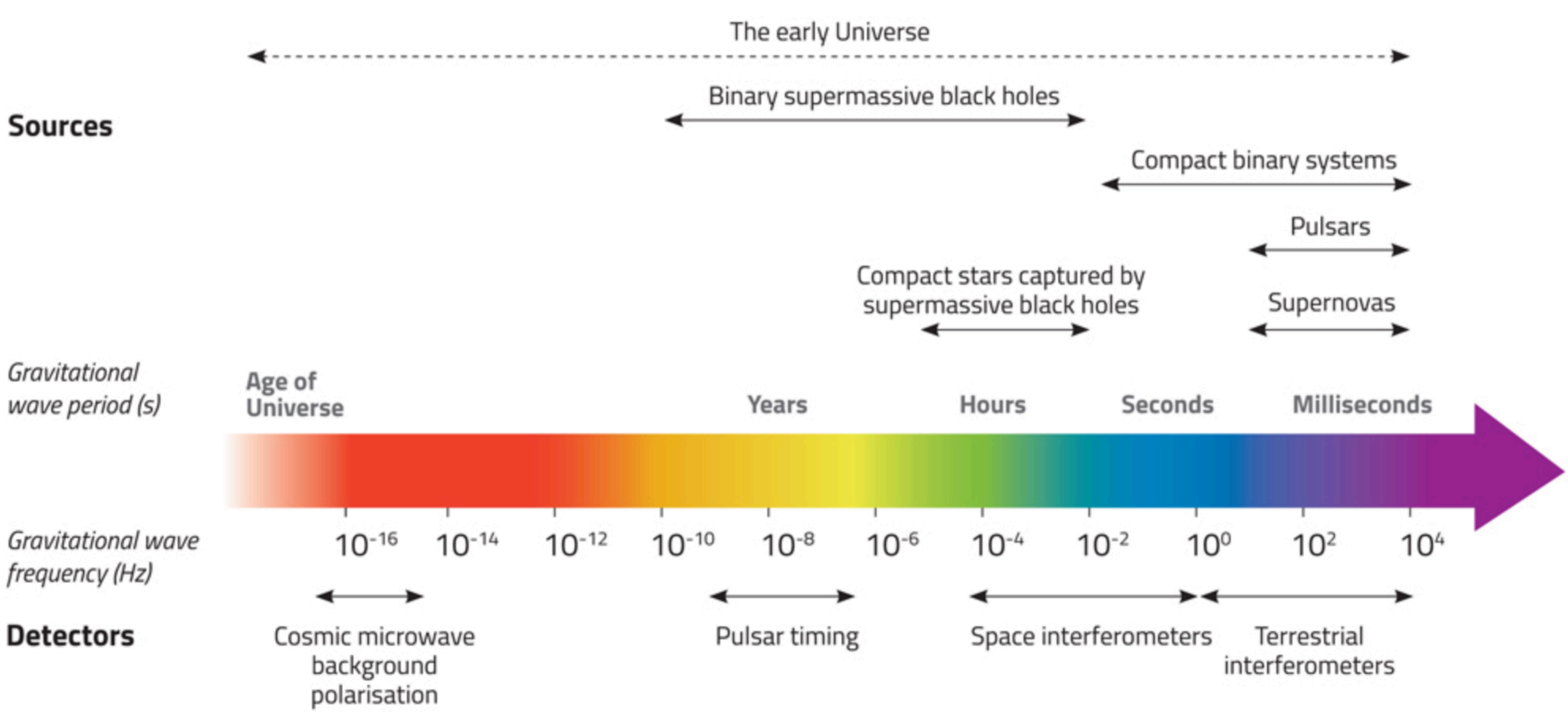

Pulsar Timing Arrays (NANOGrav)

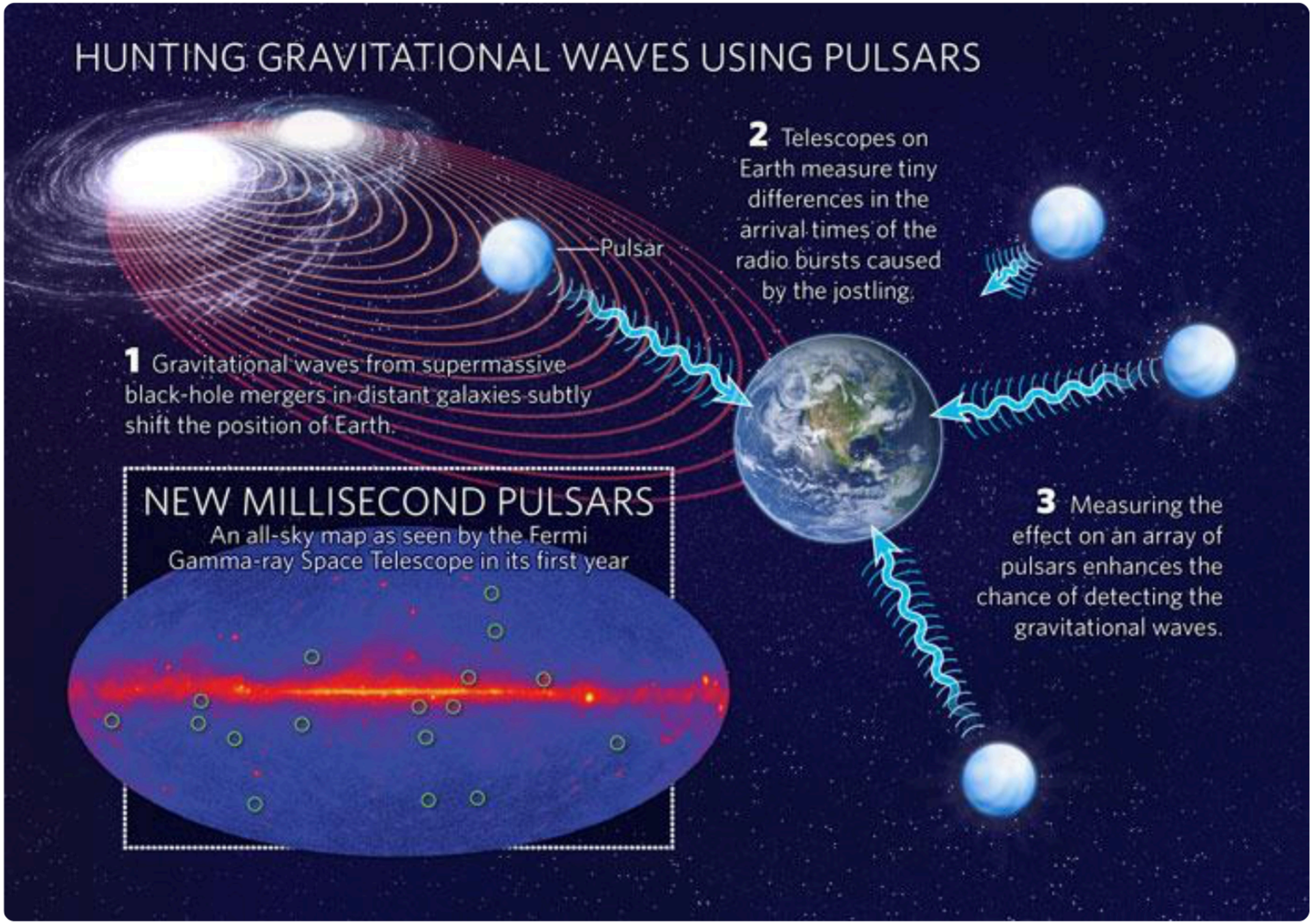

Image: A schematic pulsar timing array. (Credit: NASA/DOE/Fermi LAT Collaboration via Nature)

Primordial B-modes of the CMB = inflationary GWs

[The Primordial Inflation Polarization Explorer (PIPER)](#) - Lazear, Justin *et al.* Proc.SPIE Int.Soc.Opt.Eng. 9153 (2014) 91531L arXiv:1407.2584 [astro-ph.IM]

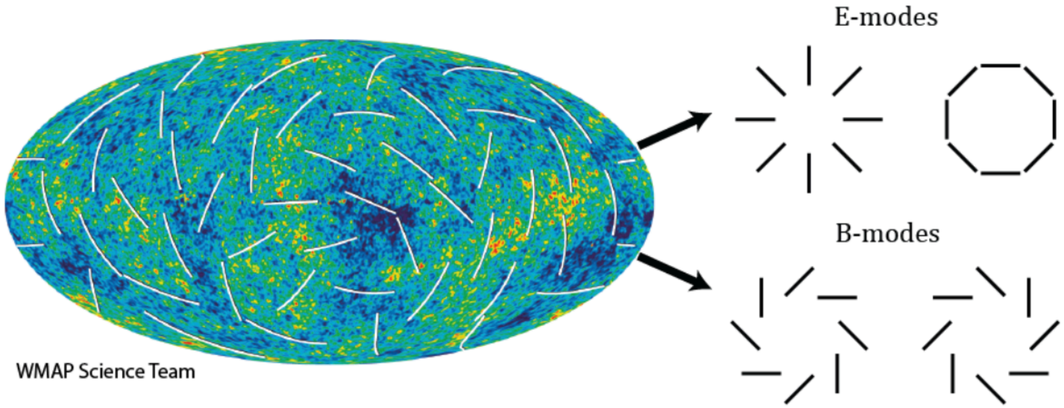

The CMB anisotropy polarization map may be decomposed into curl-free even-parity E-modes and divergence-free odd-parity B-modes. Primordial B-modes are only created by tensor perturbations (inflationary gravitational waves).

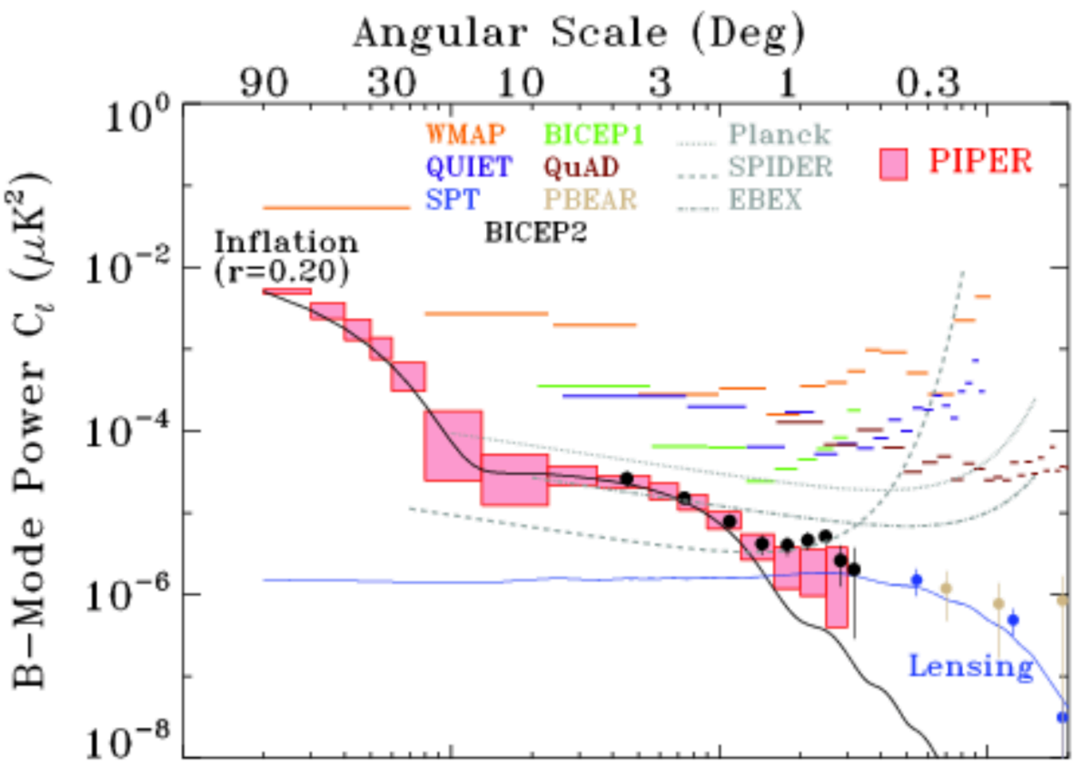

The B-mode power spectrum assuming a tensor-to-scalar ratio $r = 0.2$ from inflationary gravitational waves and gravitational lensing. The quantity being measured C_ℓ^{BB} is plotted, rather than $\ell(\ell+1)C_\ell^{BB}/2\pi$ Theories of inflation generically predict a rise in power at $\ell < 10$. \piper\ will measure the shape of the spectrum for $2 \leq \ell < 300$, encompassing the ``reionization bump'' at low $\ell$, the ``recombination bump'' at $\ell \sim 80$, as well as the lensing signal at $\ell > 200$.

But other effects could generate B-modes as well !!

1. Gravitational lensing

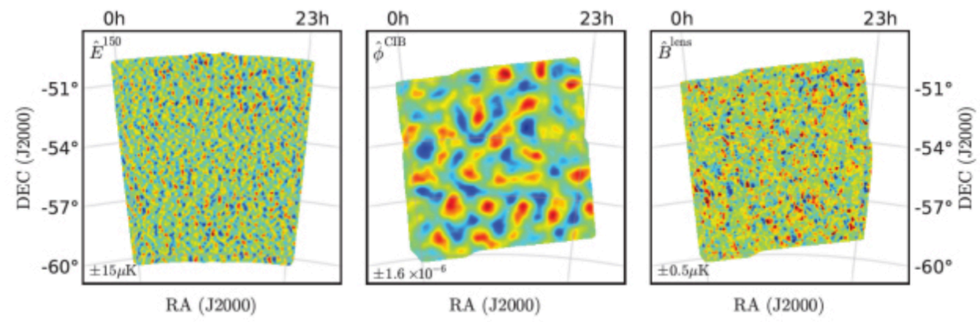

Date: 01 September 2013

Satellite: Herschel

Depicts: E-modes and B-modes in the CMB polarisation (left and right panels, respectively) and the gravitational potential of the large-scale distribution of matter that is lensing the CMB (central panel)

Copyright: Image from D. Hanson, et al., 2013, Physical Review Letters

2. Synchrotron and dust emission from our galaxy

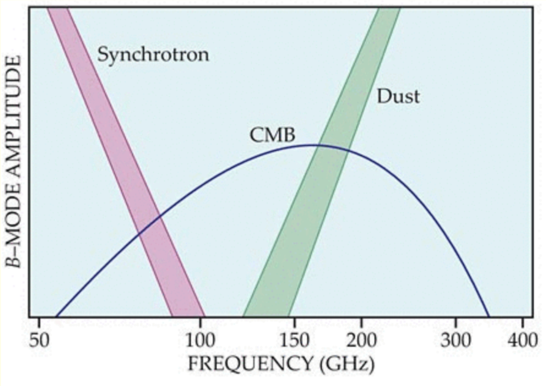

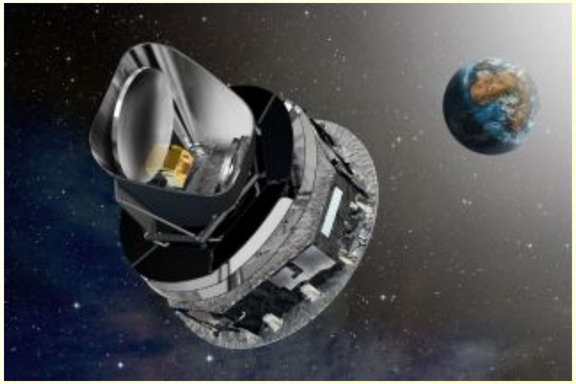

Extrapolation of Planck B-mode measurements at 353 GHz indicate that the dust contribution at 150 GHz may be appreciable in the sky region BICEP2 surveyed

The distant future